Revisiting the critical role of stabilized Criegee intermediates (sCIs) in sulfuric acid formation: coupling mechanistic updates with interpretable machine learning

Yuhuan Zhu[1], Qiang Chen[1,2], Luyan He[1], Chunlin Shang[3], Li Jiang[4], Donghong Guan[4], Guirong Yao[4], Wenkai Guo[5]

[1]Key Laboratory for Semi-Arid Climate Change of the Ministry of Education, College of Atmospheric Sciences, Lanzhou University, Lanzhou, 730000, China
[2]Lanzhou University Applied Technology Research Institude Co., Ltd, Lanzhou, 730000, China
[3]Inner Mongolia Autonomous Region Environmental Monitoring Center, Wuhai Branch, Wuhai, 016000, China
[4]Gansu Provincial Ecological and Environmental Engineering Assessment Center, Lanzhou 730000, China
[5]Faculty of Geosciences and Environmental Engineering, Southwest Jiaotong University, Chengdu, 611756, China

Correspondence to: Qiang Chen(chenqqh@lzu.edu.cn)

Abstract.

Stabilized Criegee intermediates (sCIs) provide a complementary pathway for the gas-phase oxidation of SO_2 to sulfuric acid, but the importance of this pathway under different atmospheric conditions remains insufficiently understood because kinetic parameters are still being refined and the sCI and OH pathways are strongly coupled. Here, we developed an interpretable XGBoost-based framework that integrates chemical mechanism updates, box-model simulations, and ambient observations to reevaluate the critical role of sCIs in gas-phase SO_2 oxidation. The Master Chemical Mechanism was updated to incorporate the latest IUPAC kinetic recommendations for sCI chemistry. Systematically perturbed AtChem simulations were then used to train XGBoost surrogate models, and multiple interpretation methods were applied to identify the controls on the sCI-driven SO_2 oxidation rate ($L_{SO2,sCIs}$) and the fractional sCI contribution (μ_{sCIs}), and to quantify the precursor sensitivity of the total SO_2 oxidation rate (L_{SO2}) under contrasting μ_{sCIs} regimes. The surrogate-model analysis shows that the updated mechanism substantially increases the contribution of the sCI + SO_2 pathway and redefines the relative precursor importance, with isoprene emerging as the most influential alkene. Ozonolysis-related precursors increased not only $L_{SO2,sCIs}$ but also μ_{sCIs}, because they enhanced the sCI pathway disproportionately relative to OH and, in some cases, suppressed OH-driven oxidation. In addition, high-μ_{sCIs} regimes amplified the positive responses of L_{SO2} to precursors. Observation-constrained sulfate modelling for a Wuhai summer episode further supported these regime-dependent sensitivities. These results show that distinguishing μ_{sCIs} regimes is necessary for assessing how gas-phase SO_2 oxidation can be most effectively suppressed.

1 Introduction

The environmental and climatic impacts of fine particulate matter ($PM_{2.5}$) are strongly influenced by sulfate aerosol (SO_4^{2-}), which plays a key role in regulating aerosol acidity (Yao et al., 2018), hygroscopicity (Gunthe et al., 2011), and direct radiative forcing (Quaas et al., 2022). Although a minor fraction of particulate sulfate is directly emitted from anthropogenic sources such as coal and biomass combustion (Dai et al., 2019), industrial activities (Song et al., 2025), and transportation (Cao et al., 2025), it is formed predominantly from the atmospheric oxidation of sulfur dioxide (SO_2) via gas-phase, aqueous-phase, and heterogeneous pathways (Ye et al., 2023a). During severe haze events, elevated relative humidity and aerosol loadings significantly enhance aqueous-phase and heterogeneous SO_2 oxidation. These multiphase processes dominate sulfate formation and have therefore been the focus of extensive mechanistic investigations (Cao et al., 2021). Nevertheless, the gas-phase oxidation of SO_2 remains critically important because its production, sulfuric acid (H_2SO_4), whose make it a key precursor for atmospheric new particle formation (NPF). Atmospheric nucleation and the subsequent growth of newly formed particles represent a major source of aerosol particles in terms of number concentration, and NPF has been frequently observed even if in highly polluted urban environments characterized by strong condensation sinks(Yao et al., 2018). Moreover, over the past decade, stringent emission-control policies in East Asia, particularly in China, have substantially reduced $PM_{2.5}$ concentrations (Geng et al., 2021), thereby weakening conditions favorable for aqueous-phase and heterogeneous sulfate formation. In this progressively cleaner atmosphere, the relative importance of gas-phase pathways is expected to increase (Wang et al., 2025). Therefore, under increasingly stringent air pollution control targets (WHO, 2021), the role of SO_2 gas-phase oxidation pathways in secondary aerosol production is expected to become more important and warrants further investigation.

Hydroxyl radicals (OH) have long been recognized as the dominant oxidant in gas-phase SO_2 oxidation. Since the pioneering work of Cox and Penkett et al. (1971) first demonstrated that Criegee intermediates (zwitterionic carbonyl oxides, $R_1R_2C{=}O^+{-}O^-$) react with SO_2 in the gas phase, extensive laboratory and theoretical studies (Taatjes et al., 2013; Vereecken et al., 2012) have advanced understanding of the formation, stabilization, and fate of CIs. Stabilized Criegee intermediates (sCIs) are therefore increasingly considered an important complementary pathway for the gas-phase SO_2 oxidation and a potentially significant contributor to H_2SO_4 formation. Multiple field observation studies conducted in the boreal forests in Finland (Mauldin et al., 2012), the SMEAR II and Hohenpeissenberg stations in Germany (Boy et al., 2013), in urban Beijing (Guo et al., 2021), and at a remote Mediterranean site strongly influenced by biogenic VOC emissions (Kukui et al., 2021a) suggest that sCIs can provide an additional, environment-dependent pathway for SO_2 oxidation. Notably, as the direct measurement of atmospheric sCIs concentrations remains a formidable challenge, observational studies have primarily relied on the analysis of precursors and OH radical concentrations to provide qualitative evidence. Consequently, numerical simulations grounded in CIs chemical kinetics are indispensable for quantifying the contribution of sCIs to the gas-phase SO_2 oxidation rate.

To date, numerical modeling studies have extensively evaluated the contribution of sCIs to SO_2 oxidation across a broad range of spatial scales and environmental conditions. For instance, utilizing a steady-state approximation, Khan et al. (2017) estimated that the OH-driven SO_2 oxidation rate in urban London (0.64 Tg/year) was approximately 17 times that of the sCI pathway (37.6 Gg/year). However, proxy calculations of H_2SO_4 concentrations have revealed pronounced regional disparities: at the semi-pristine boreal forest site in Hyytiälä, the photochemical pathway (SO2 + OH) and the alkene ozonolysis pathway (SO_2 + sCIs) accounted for approximately 34% and 60% of H_2SO_4 production, respectively, whereas in heavily polluted Beijing, the corresponding proportions shifted to 28% and 22% (Dada et al., 2020). Vereecken et al. (2017) predicted that in equatorial regions, the contribution of sCIs to the gas-phase conversion of SO_2 to sulfuric acid could reach up to 75%. Furthermore, simulations using the STOCHEM-CRI global atmospheric chemistry and transport model demonstrated (Khan et al., 2018) that the SO_2 oxidation contribution from sCIs significantly exceeds that of OH radicals in terrestrial rainforests and high-latitude boreal forests. This pronounced variability is primarily driven by two intertwined factors. First, considerable uncertainty in numerical simulations arises from inherent limitations in our understanding of CIs chemical kinetics. With continuous breakthroughs in monitoring technologies, the scientific understanding of CI evolution processes is dynamically evolving, resulting in discrepancies in the reaction rate coefficients incorporated into models across different periods. Notably, the unimolecular decomposition rates of CIs/sCIs and the bimolecular reaction rates of sCIs with water monomers and dimers (H_2O/$(H_2O)_2$) exert a decisive influence on numerical calculations (Sarwar et al., 2014). For example, a modeling study under summer conditions in the eastern United States demonstrated that once the competitive reaction between sCIs and H_2O/$(H_2O)_2$ was introduced, the sCI-driven enhancement in surface sulfate plummeted from 18% to less than 0.5% (Li et al., 2013). Similarly, in simulations of nocturnal power plant plumes in the southeastern US, whether CI thermal decomposition was considered led to a seven-fold difference in the estimated contribution to secondary sulfate aerosol (SSA) formation (Meidan et al., 2019). Second, pronounced regional heterogeneity in precursor composition, such as biogenic isoprene and monoterpenes in forested regions and complex anthropogenic alkene mixtures in urban areas, together with differences in relative humidity and NO_x levels, leads to highly variable sCI production and scavenging fluxes. While existing studies have made progress in quantifying the contribution of sCIs to gas-phase SO_2 oxidation in specific environments and identifying their precursors, the relationship between sCIs and their precursors remains unclear. Consequently, a systematic understanding of the critical driving factors dictating the relative contribution of sCIs is still lacking. Moreover, the production and loss processes of OH and sCIs are not mutually independent; rather, they are deeply coupled within the underlying chemical mechanisms (Zhu et al., 2023). This coupled nature dictates that when evaluating the drivers controlling the contribution of the sCIs+SO_2 pathway, their concurrent impacts on the OH+SO_2 pathway and the overall SO_2 oxidation rate cannot be overlooked. Fundamentally, the interplay between precursor abundances and competitive sinks determines the fractional contribution of the sCIs pathway. Yet, how this interplay shapes the sensitivity of the total gas-phase SO_2 oxidation to environmental drivers has received remarkably little attention. In particular, it remains elusive how the dominant controlling factors and their directional impacts shift as the atmospheric gas-phase SO_2 oxidation regime transitions from being strictly OH-dominated to being co-driven by both OH and sCIs.

To this end, this study presents a systematic assessment of the role of sCIs in atmospheric SO_2 gas-phase oxidation. As a prerequisite for all subsequent analyses, we first updated the gas-phase kinetics of Criegee intermediates in the Master Chemical Mechanism (MCM v3.3.1, via website: www.mcm.york.ac.uk) using the latest evaluated rate coefficients recommended by the International Union of Pure and Applied Chemistry (IUPAC), thereby minimizing the propagation of mechanistic uncertainties into our conclusions. Utilizing an atmospheric box model coupled with this revised mechanism, we integrated interpretable machine learning techniques to quantify the importance of key controlling factors on sCI-mediated SO_2 oxidation. Building upon this insight, we employed a robust experimental design to construct a machine learning surrogate model capable of predicting sCI contributions across diverse and highly variable environmental conditions. Furthermore, analytical methods, including SHAP, Sobol sensitivity analysis, Partial Dependence Plots (PDPs), and individual conditional expectation (ICE) plots, were utilized to quantify how these factors dictate the relative contribution of sCIs, and to elucidate the differential sensitivities of total SO_2 oxidation under high- and low-sCI contribution regimes. Finally, leveraging online hourly observational data of atmospheric pollutants, we assessed the disparities in their sensitivity relationships with SO_4^{2-} across varying sCI contribution levels, ultimately validating the reliability of our box model-derived surrogate model.

2 Data and methodology

2.1 Updates to alkene ozonolysis and Criegee intermediate chemistry in MCM v3.3.1

The Master Chemical Mechanism (MCM v3.3.1; available via http://mcm.york.ac.uk) is a near-explicit chemical mechanism describing the gas-phase oxidation of 143 volatile organic compounds (VOCs) to carbon dioxide (CO_2) and water (H_2O). In MCM v3.3.1, the rate coefficients and associated reaction mechanisms for alkene ozonolysis (alkenes + O_3) follow the recommendations of Jenkin et al. (1997, 2015) and Saunders et al. (2003). Although the mechanism provides a detailed representation of the formation, loss, and subsequent evolution of CIs, several key rate coefficients and parameters deviate significantly from the latest IUPAC recommendations (Cox et al., 2020). Furthermore, critical chemical pathways are currently omitted, including specific fates of CIs, unimolecular decomposition pathways of sCIs, reactions with water dimers ($(H_2O)_2$), and the distinct reactivities of different sCI stereoisomers. To address these limitations, we updated the gas-phase alkene + O_3 chemistry within MCM v3.3.1, based primarily on the current IUPAC recommendation. These modifications consist of updating the alkene ozonolysis rate coefficients ($k_{O3+alkene}$), OH yields ($Y_{i,OH}$), sCIs yields ($Y_{i,sCI}$), and sCI bimolecular reaction rate coefficients (k_b), alongside accounting for the sCI unimolecular decomposition pathways and adding the sCI + $(H_2O)_2$ reactions. Specifically, the branching ratios for the unimolecular decomposition (or isomerization) pathways of both CIs and sCIs were constrained by, and derived from, the reported yields of OH and other respective products. For sCIs exhibiting stereoisomerism (such as CH_3CHOO, C_2H_5CHOO, and the C4 intermediates formed from isoprene ozonolysis), the Z-stereoisomers are assumed to predominantly undergo rapid unimolecular decomposition under tropospheric conditions, rendering their contributions to bimolecular reactions negligible. Consequently, in the updated

mechanism (designated as MCM v3.3.1g), stereoisomeric sCIs participating in bimolecular reactions are explicitly represented by their E-stereoisomers. The unimolecular decomposition pathways of the sCIs and the decomposition (or isomerization) channels of their corresponding chemically activated CIs are treated in combination. The kinetic parameters and product yields for the alkene ozonolysis reactions before and after the mechanism updates are summarized in Tables S1 and S2, while the complete set of updated reaction equations and explicit branching ratios are detailed in Table S3. These mechanism updates were applied to C_1-C_4 Criegee intermediates, which are widely recognized to play a critical role in tropospheric chemistry.

The concentration of $(H_2O)_2$ is determined assuming a rapid thermal equilibrium between water monomers and dimers. Given this fast atmospheric exchange, the dimer concentration is considered to be in thermodynamic equilibrium with the monomer, as expressed in Eq. (1):

$$K_{eq}^{D} = \frac{[(H_2O)_2]}{[H_2O]^2} \quad (1)$$

where K_{eq}^{D} is the temperature-dependent equilibrium constant for dimer formation (Scribano et al., 2006). Following the methodology of Lade et al. (2024), the reaction of sCIs with water dimers is parameterised using an effective third-order rate coefficient, k_{eff}, such that the total reaction rate (r) is given by Eq. (2):

$$r = k_{b,dimer}[sCI][(H_2O)_2] = k_{b,dimer} \times K_{eq}^{D}[sCI][H_2O]^2 = k_{eff}[sCI][H_2O]^2 \quad (2)$$

k_{eff} is defined as the product of the bimolecular rate coefficient for the sCI + $(H_2O)_2$ reaction ($k_{b,dimer}$) and K_{eq}^{D}. To ensure accuracy in calculating K_{eq}^{D}, thermochemical data were retrieved from the Active Thermochemical Tables (ATcT). Standard Gibbs free energies of formation ($\Delta_f G_T^{\circ}$) for both the water monomer and dimer were extracted from Tables 1 and 3 in Ruscic (2013). These discrete data points were then utilized to calculate the reaction Gibbs free energy ($\Delta_r G_T^{\circ}$) over the temperature range of 200 to 360 K, which spans the typical conditions of the troposphere. The temperature dependence of K_{eq}^{D} was subsequently obtained via a linear regression of $ln\left(K_{eq}^{D}\right)$ as a function of $\frac{1}{T}$, yielding the following Arrhenius-type parameterization in Eq. (3):

$$K_{eq}^{D}(T) = Aexp\left(\frac{B}{T}\right) \quad (3)$$

where the coefficients A and B represent the intercept and slope derived from the fitting procedure respectively, with A = 1.15×10^{-23} cm^3 molecule^{-1} and B = 1549.32 K.

2.2 Box model configuration and observation data

2.2.1 AtChem model setup and chemical diagnostics

AtChem (Sommariva et al., 2020), an open-source zero-dimensional atmospheric box model, was used in this study to simulate the gas-phase chemical evolution of SO_2, sCIs, and their precursors. The AtChem model is coupled with MCM v3.3.1 and MCM v3.3.1g (see Sect. 2.1). H_2O concentrations for sCIs loss reactions are calculated from relative humidity, temperature, and atmospheric pressure.

Two types of AtChem simulations were performed in this study. The first type used an unconstrained configuration, in which the initial concentrations of selected chemical species were prescribed and allow to evolved according to the chemical mechanism without time-varying constraints. This configuration was used in Sect. 3.1 to quantify the oxidation capacity of sCIs derived from the ozonolysis of specific alkenes, including ethylene, propene, but-1-ene, *trans*-but-2-ene, *cis*-but-2-ene, 2-methylpropene, and isoprene. The second type used a constrained configuration, in which selected trace gases, meteorological parameters, and photolysis frequencies were prescribed as hourly time-varying inputs from observational data or designed perturbation scenarios. This configuration was used in Sects. 3.2 and 3.3 to evaluate the role of sCIs in gas-phase SO_2 oxidation under atmospherically relevant conditions. A spin-up period of 2-3 days was implemented to initialize reactive free radicals and intermediates, such as OH, HO_2, RO_2, and sCIs, allowing them to reach realistic steady-state concentrations.

Chemical production and loss rates were quantified using the Rate of Production/Destruction Analysis (ROPA/RODA) within AtChem (Sommariva et al., 2020). The gas-phase SO_2 oxidation rate by sCIs was defined according to Eq. (4):

$$L_{SO_2,sCIs} = \sum_i k_{sCI+SO_2}[sCI_i][SO_2], \quad (4)$$

where i denotes individual sCI species. The OH-driven SO_2 oxidation rate was defined as Eq. (5):

$$L_{SO_2,OH} = k_{OH+SO_2}[OH][SO_2]. \quad (5)$$

The total gas-phase SO_2 oxidation rate and the fractional sCI contribution were then calculated as Eq. (6) and Eq. (7):

$$L_{SO_2} = L_{SO_2,sCIs} + L_{SO_2,OH}. \quad (6)$$

$$\mu_{sCIs} = \frac{L_{SO_2,sCIs}}{L_{SO_2}}. \quad (7)$$

Here, $L_{SO_2,sCIs}$ and μ_{sCIs} provide complementary perspectives on the absolute rate and fractional contribution of the sCI pathway.

2.2.2 Observation data

The observational data used in this study were obtained from the automatic monitoring system at the Wuhai City Atmospheric Environment Super Monitoring Station from 9 October 2019 to 30 June 2022. Wuhai is a semi-arid coal-chemical industrial city in Inner Mongolia, China, relatively high SO_2 emissions, abundant anthropogenic VOCs including alkene, frequent O_3 pollution, and comparatively dry atmospheric conditions. The dataset includes air pollutants ($PM_{2.5}$, carbon monoxide (CO), SO_2, nitrogen dioxide (NO_2), and ozone (O_3)), meteorological variables (wind speed (WS), temperature (T), pressure (P), relative humidity (RH)), water-soluble inorganic ions (including NO_3^- and SO_4^{2-}), elemental components (including Fe), VOCs, and photolysis frequencies. $PM_{2.5}$, NO_2, SO_2, CO, and O_3 were measured using a Metone BAM-1020 $PM_{2.5}$ Monitor, an API T201 NH_3-NO_x Analyzer, an API T100 SO_2 Analyzer, an API T300 CO Analyzer, and an API T400 O_3 Analyzer, respectively. VOCs were measured using an ENTECH BCT-7800 VOCs Analyzer. Water-soluble inorganic ions were measured using a Metrohm MARGA ADI 2080 online ion chromatograph, and elemental components were measured using a CES Xact-625 atmospheric heavy metal analyzer. Meteorological variables (T, RH, P, WS) were

measured using a Lufft WS601-UMB six-parameter meteorological sensor. Photolysis frequencies were measured using a Metcon UF-CCD photolysis spectroradiometer. The observational data had an hourly time resolution and were screened for invalid values. Short missing intervals were linearly interpolated when appropriate, whereas longer gaps were excluded from the analysis.

2.3 Machine learning model and interpretation framework

An interpretable machine learning (ML) framework was developed to systematically evaluate the role of sCIs in SO2 oxidation in this study, encompassing model development, validation, and interpretation. The learning algorithm throughout is Extreme Gradient Boosting (XGBoost) (Chen and Guestrin, 2016), which constructs an additive ensemble of regression trees by iteratively minimising a regularised loss function, with each successive tree fitted to the negative gradients of its predecessors. This formulation enables nonlinear responses and predictor interactions to be represented far more flexibly than by a single regression tree. Regularisation, subsampling, cross-validation, and early stopping were applied to suppress overfitting, and hyperparameters were tuned by random search or Bayesian optimisation. The same sampling-training-testing workflow was applied to every model in this study. Two classes of XGBoost model were constructed (using the XGBoost Python package, version 2.1.3; https://github.com/dmlc/xgboost): surrogate models trained on AtChem simulations of chemical evolution, and an observation-based model trained on ambient measurements. Four complementary interpretations were using to explain the XGBoost models outputs, including SHAP (SHapley Additive exPlanations), Sobol sensitivity analysis, partial dependence plots (PDPs) and individual conditional expectation (ICE) plots.

2.3.1 Model Development Details

There are three surrogate models developing based on SO_2 gas-phase oxidation simulations from AtChem, which successively quantify the key controls on the sCI oxidation capacity on SO2, identify the atmospheric conditions under which the sCI pathway becomes important, and investigate the impact of its importance on the sensitivity of total SO2 oxidation. And an observation-based model that assesses whether the sensitivities inferred from the surrogates are echoed in ambient measurements. These XGBoost models are introduced in turn below.

First, a surrogate model was developed to emulate the sCI-mediated SO_2 oxidation rate ($L_{SO2,sCIs}$), with SHAP analysis applied to diagnose the contributions of its key controlling factors — the principal sCI precursors and competing sinks (most notably NO_2, H_2O, and $(H_2O)_2$). The feature set therefore comprises O_3, RH, NO_2, and six alkene precursors: ethene, propene/but-1-ene, *trans*-but-2-ene, *cis*-but-2-ene, 2-methylpropene, and isoprene, where propene and but-1-ene are merged into a single feature owing to the close similarity of their ozonolysis mechanisms. To capture individual perturbations and interactions across all features, 3898 simulation scenarios were designed spanning the prescribed feature ranges. In each scenario, the feature values prescribe the initial input concentrations for a 1h unconstrained AtChem simulation, with SO_2 held constant; the mean $L_{SO2,sCI}$ over the simulated hour, obtained under both MCM v3.3.1 and v3.3.1g, served as the target output. The resulting feature matrix and corresponding simulation outputs together constitute the training dataset for the

surrogate model. The prescribed feature ranges, full scenario design, training details, and model performance are provided in Text S1.

Second, to identify the atmospheric conditions that favour sCI contribution to total gas-phase SO_2 oxidation, a surrogate model was developed to predict the fractional importance of the sCI pathway (μ_{sCIs}), combined with Sobol sensitivity analysis, PDPs, and ICE plots. Unlike $L_{SO2,sCIs}$, which depends solely on sCI production and loss, μ_{sCIs} is also governed by the competing OH-driven oxidation pathway and therefore requires a feature set that captures both sCI and OH chemistry. Accordingly, the feature set comprises O_3, NO_x, NO_2 fraction ($NO_2\% = NO_2/NO_x$), total VOC concentration (VOCs), alkene fraction (alkene% = ∑alkenes/VOC), RH, and the Aggregated Reactivity Index (ARI). The NO_x-NO_2% and VOC-alkene% pairs jointly characterise the oxidant state and reactive VOC composition while minimising multicollinearity among features. ARI is an ordinal variable encoding the sCI-oxidation potential of the prevailing alkene mixture, derived directly from the importance ranking of alkene features established by the $L_{SO2,sCIs}$ surrogate model. The generated training samples for this surrogate differs from that of the $L_{SO2,sCI}$s model. Rather than prescribing initial concentrations, the feature values here represent normalised scaling factors applied to time-varying constraints, as the AtChem model was run in a constrained configuration. The baseline constraints are the three-year mean diurnal cycles of hourly observations at the Wuhai supersite (Sect. 2.1), and the perturbation range of each feature spans the 5th-95th percentile range of the observed concentrations (normalised range is [0,1]); ARI, as an ordinal discrete variable, is the sole exception and takes integer values of 0, 1, or 2 corresponding to the three tiers of sCI-oxidation potential. Because photolysis frequencies play a decisive role in OH production and radical cycling, daytime and nighttime conditions were treated as entirely separate modelling problems, with target time periods are CST 08:00-18:00 and 22:00-05:00, respectively. For each scenario, the constraints of the target period were adjusted according to the prescribed feature values while all remaining constraints (non-feature variables) were held at baseline; a constrained AtChem simulation under MCM v3.3.1g then yielded the mean μ_{sCIs} and L_{SO2} over the target period as the target outputs. The resulting feature matrix and simulation μ_{sCIs} values together constitute the training datasets for the daytime and night-time μ_{sCIs} surrogate models. Dividing this dataset into low- and high-μsCIs subsets based on the median of μ_{sCIs}, a further pair of surrogate models was developed to predict the total gas-phase SO_2 oxidation rate (L_{SO2}) separately each regime, combined with partial dependence analysis to assess whether the sensitivity of L_{SO2} to each feature depends on the relative importance of the sCI pathway. The baseline constraints, the mapping from normalised feature values to constraint magnitudes, full scenario design, training details, and model performance are provided in Text S2.

Finally, to assess whether the regime-dependent sensitivities inferred from the surrogate models are also expressed in the real atmosphere, we developed an observation-based model trained on ambient observations from the Wuhai supersite (9 October 2019 to 30 June 2022, hourly resolution) to predict SO_4^{2-}. The features including $PM_{2.5}$, NO_3^-, SO_2, O_3, total VOCs, alkene%, NO_x, NO_2%, RH, wind speed, and Fe, selected to represent sulfate precursor abundance, photochemical oxidation capacity, aerosol loading, secondary inorganic aerosol formation, meteorological conditions, gas-phase and aqueous-phase oxidation pathways. SHAP analysis was applied to evaluate the differential contributions of key features to SO_4^{2-} under contrasting

μ_{sCIs} regimes, enabling comparison with the regime-dependent sensitivities diagnosed from the AtChem-based surrogate models. Training details and model performance are provided in Text S3.

2.3.2 Model Interpretation Methods

In this study, XGBoost was not used merely as a black-box surrogate for predicting chemical reaction rates or target pollutant concentrations. Instead, it served as a computationally efficient emulator of the box-model simulations, enabling systematic sensitivity analysis and interpretation of the chemical response within the prescribed parameter space. To interpret the trained XGBoost models, we combined SHAP analysis, Sobol sensitivity analysis, partial dependence plots (PDPs), and individual conditional expectation (ICE) plots. These approaches provide complementary perspectives. SHAP values were used to quantify the relative importance and direction of predictor effects at both individual-sample and aggregate levels, while SHAP interaction values were used to diagnose key two-factor interactions. Sobol sensitivity analysis provided a variance-based decomposition of the model output, separating the independent contribution of each input factor from interaction-driven contributions. PDPs were used to visualize the average nonlinear response of the model output to selected predictors and to identify potential thresholds, whereas ICE plots were used to examine whether these responses were consistent across individual samples or varied among different chemical regimes. For models trained on controlled numerical experiments, these interpretation results were treated as model-estimated chemical sensitivities constrained by the updated chemical mechanism and the sampled parameter space. For the model trained on ambient observations, however, SHAP-based interpretations were interpreted as statistical associations used to evaluate consistency with the process-model results, rather than as direct causal attribution.

(1) SHAP (SHapley Additive exPlanations) is a game-theoretic approach for interpreting machine learning model predictions (Lundberg and Lee, 2017; Lundberg et al., 2018). Each input feature is treated as a "player" in a cooperative game, and the model prediction for any individual sample is expressed as an additive decomposition of per-feature contributions. Specifically, for a sample x_i with N features, the predicted value $f(x_i)$ is decomposed as Eq. (8):

$$f(x_i) = \phi_0 + \sum_{j=1}^{N} \phi_j(f, x_i) \quad (8)$$

Where $\phi_0 = \mathrm{E}[f(x)]$ is the base value, i.e., the expected model output averaged over the entire dataset, and $\phi_j(f, x_i)$ is the SHAP value of feature j for sample x_i, quantifying the contribution of feature j to the deviation of $f(x_i)$ from ϕ_0. The SHAP value $\phi_j(f, x_i)$ is computed as the weighted average marginal contribution of feature j across all possible subsets of the remaining features Eq. (9):

$$\phi_j(f, x_i) = \sum_{S \subseteq F \setminus \{j\}} \frac{|S|!(|F|-|S|-1)!}{|F|!} [f(S \cup \{j\}) - f(S)] \quad (9)$$

Where F is the full set of features, S denotes a subset of features that excludes feature j, and $f(S)$ denotes the conditional expectation of the model output given the features in S. The sign of $\phi_j(f, x_i)$ indicates the direction of the feature effect for a specific sample (positive: the feature j increases the predicted value relative to the baseline; negative: it decreases

it), and the magnitude indicates the strength of that effect. For XGBoost models, SHAP values are computed exactly and efficiently using the TreeExplainer algorithm (Lundberg et al., 2020).

The global importance of feature *j* is summarized by its mean absolute SHAP value (Eq. (10)):

$$\overline{|\phi_j|} = \frac{1}{n}\sum_{i=1}^{n}|\phi_j(f, x_i)| \quad (10)$$

where n is the total number of samples. $\overline{|\phi_j|}$ represents the average magnitude of feature *j*'s contribution to model predictions across the dataset and is used to rank features by their global importance.

Pairwise feature interactions are further quantified via SHAP interaction values. The mean absolute interaction value between features *i* and *j* is defined as Eq. (11):

$$\overline{|\phi_{pq}|} = \frac{1}{n}\sum_{i=1}^{n}|\phi_{pq}(f, x_i)| \quad (11)$$

Where $\phi_{pq}(f, x_i)$ is the SHAP interaction value between features p and q for sample x_i, representing the joint contribution of the feature pair that cannot be attributed to either feature's individual main effect.

(2) A variance-based global sensitivity analysis was performed using the Sobol method (Saltelli et al., 2010; Sobol, 2001). Sobol analysis apportions the total variance of the model output to individual input factors and their interactions across the prescribed input domain, thereby providing a distribution-free measure of global sensitivity that is independent of the training data distribution.

For a model output $Y = f(x)$ with N input factors(features) x_1, x_2, …, x_N, the total output variance Var (Y) can be decomposed into contributions from individual factors and their interactions as Eq. (12):

$$Var(Y) = \sum_{j=1}^{N} V_j + \sum_{j<k} V_{jk} + \ldots \quad (12)$$

where $V_j = Var_{x_j}\left[\mathrm{E}_{x_{\sim j}}\left(Y|x_j\right)\right]$ is the variance attributable solely to x_j, and V_{jk} captures the additional variance arising from interactions among factors.

Two Sobol sensitivity indices were computed for each input factor. The first-order index S_j quantifies the independent main effect of x_j on the output variance as Eq. (13):

$$S_j = \frac{V_j}{Var(Y)} \quad (13)$$

The total-order index S_{Tj} encompasses the main effect of x_j together with all higher-order interaction terms involving x_j as Eq. (14):

$$S_{T_j} = \frac{\mathrm{E}_{x_{\sim j}}\left[Var_{x_j}\left(Y|x_{\sim j}\right)\right]}{Var(Y)} = 1 - \frac{\mathrm{Var}_{x_{\sim j}}\left[E_{x_j}\left(Y|x_{\sim j}\right)\right]}{Var(Y)} \quad (14)$$

where $x_{\sim j}$ denotes all input factors except x_j. By construction, both indices lie in [0, 1]. The difference (S_{Tj} - S_j) provides a direct measure of the cumulative contribution of x_j to interaction effects: values of S_{Tj} substantially exceeding S_j indicate that x_j participates strongly in non-additive interactions with other predictors, an effect that cannot be detected from main-effect rankings alone.

Input samples for the Sobol sensitivity analysis were generated using the Saltelli quasi-random sampling scheme (Saltelli, 2002). A base sample size of 32768 was used, resulting in approximately 524000 model evaluations for the seven input variables. This evaluation budget was computationally tractable because the trained XGBoost surrogate model replaced the more expensive box-model simulations. For the ARI variable, which was encoded as an ordinal integer with values of 0, 1, and 2, the continuous Saltelli samples were rounded to the nearest integer and clipped to the valid range to match the training data representation. Sobol indices were estimated using the SALib library (Herman and Usher, 2017), with 95 % bootstrap confidence intervals reported for all indices.

(3) Partial dependence plots (PDPs) were used to visualize the marginal relationship between selected predictors and target variable after averaging out the influence of all other features. For a feature of interest x_p and complementary feature set x_c, the one-dimensional partial dependence function is defined as Eq. (15):

$$\hat{f}_p(x_p) = \mathrm{E}_{x_c}[f(x_p, x_c)] \approx \frac{1}{n}\sum_{i=1}^{n} f(x_p, x_c^{(i)}) \quad (15)$$

where the expectation is approximated by averaging the surrogate model's predictions over all n training samples while fixing x_p at a grid of target values.

Two-dimensional PDPs were further constructed for eight selected pairs of features to quantify joint interaction effects. For a predictor pair (x_p, x_q), the two-dimensional partial dependence function is defined as Eq. (16):

$$\hat{f}_{pq}(x_p, x_q) = \mathrm{E}_{x_c}[f(x_p, x_q, x_c)] \approx \frac{1}{n_{MC}}\sum_{i=1}^{n_{MC}} f(x_p, x_q, x_c^{(i)}) \quad (16)$$

(4) Individual conditional expectation (ICE) plots were used to complement the PDP analysis by examining the model response at the individual-sample level (Goldstein et al., 2015). Whereas PDPs describe the average marginal effect of a predictor after averaging over all samples, ICE plots display the conditional response curve for each individual sample while varying the feature of interest and holding the remaining features fixed at their observed values. This allows response heterogeneity across different chemical regimes to be examined and helps determine whether the averaged PDP response is representative of most samples or is driven by a subset of conditions. In this study, ICE plots were used to assess the consistency of nonlinear predictor effects, identify regime-dependent responses, and detect cases where opposing individual responses may be obscured in the averaged PDP.

3 Results and Discussion

3.1 Effects of key controlling factors on sCIs-mediated SO_2 oxidation

sCIs are short-lived reactive intermediates generated from the ozonolysis of alkenes. Their contribution to gas-phase SO_2 oxidation is governed jointly by their atmospheric steady-state concentration and their bimolecular rate coefficient with SO_2. The steady-state concentration is itself determined by the initial ozonolysis rate coefficient, the total sCI yield, and the structure-dependent reactivities of individual sCI species toward other competing sinks—most notably H_2O, $(H_2O)_2$, and NO_2—which collectively regulate the fraction of sCIs available to react with SO_2. To capture this integrated response, we

introduce the sCI-driven SO_2 oxidation rate, $L_{SO2,sCIs}$, as a comprehensive metric that simultaneously accounts for sCI production and the effective SO_2 oxidation capacity. Figures 1a and 1b illustrate that within both MCM v3.3.1 and MCM v3.3.1g, alkenes and O_3 concentrations are positively associated with $L_{SO2,sCIs}$, whereas marked negative correlations are observed for RH and NO_x. This pattern is consistent with the expected roles of alkenes and O_3 driving sCI production, while $H_2O/(H_2O)_2$ and NO_2 act as competing sinks that reduce the fraction of sCIs available to react with SO2. Notably, updating the mechanism leads to a pronounced increase in the magnitude of the absolute SHAP (|SHAP|) values across all features (Fig. 1c), with the average |SHAP| values increasing from 211.9-11,177.3 molecule·cm^{-3}·s^{-1} in MCM v3.3.1 to 694.0-30429.5 molecule·cm^{-3}·s^{-1} in MCM v3.3.1g. This indicates that the updated mechanism yields a substantially stronger sensitivity of $L_{SO2,sCIs}$ to perturbations in environmental and precursor variables, i.e., the same change in a feature variable produces a larger response in $L_{SO2,sCIs}$. Importantly, the mechanism update does not simply scale all responses uniformly; it also changes the relative attributed importance of individual alkenes (Fig. 1d). In MCM v3.3.1, the alkene importance ranking is dominated by trans-2-butene (21.5%) > cis-2-butene (17.6%) > isoprene (9.5%) > isobutene (4.3%) > ethylene (0.7%) > propylene/butene (0.5%). In MCM v3.3.1g, isoprene becomes the most important alkene feature (23.8%), followed by trans-2-butene (11.0%), cis-2-butene (9.7%), and isobutene (6.0%), while ethene (0.9%), and propene/1-butene (0.7%) remain minor contributors. The approximately sixfold increase in the attributed importance of isoprene (Hata et al., 2023; Newland et al., 2015).

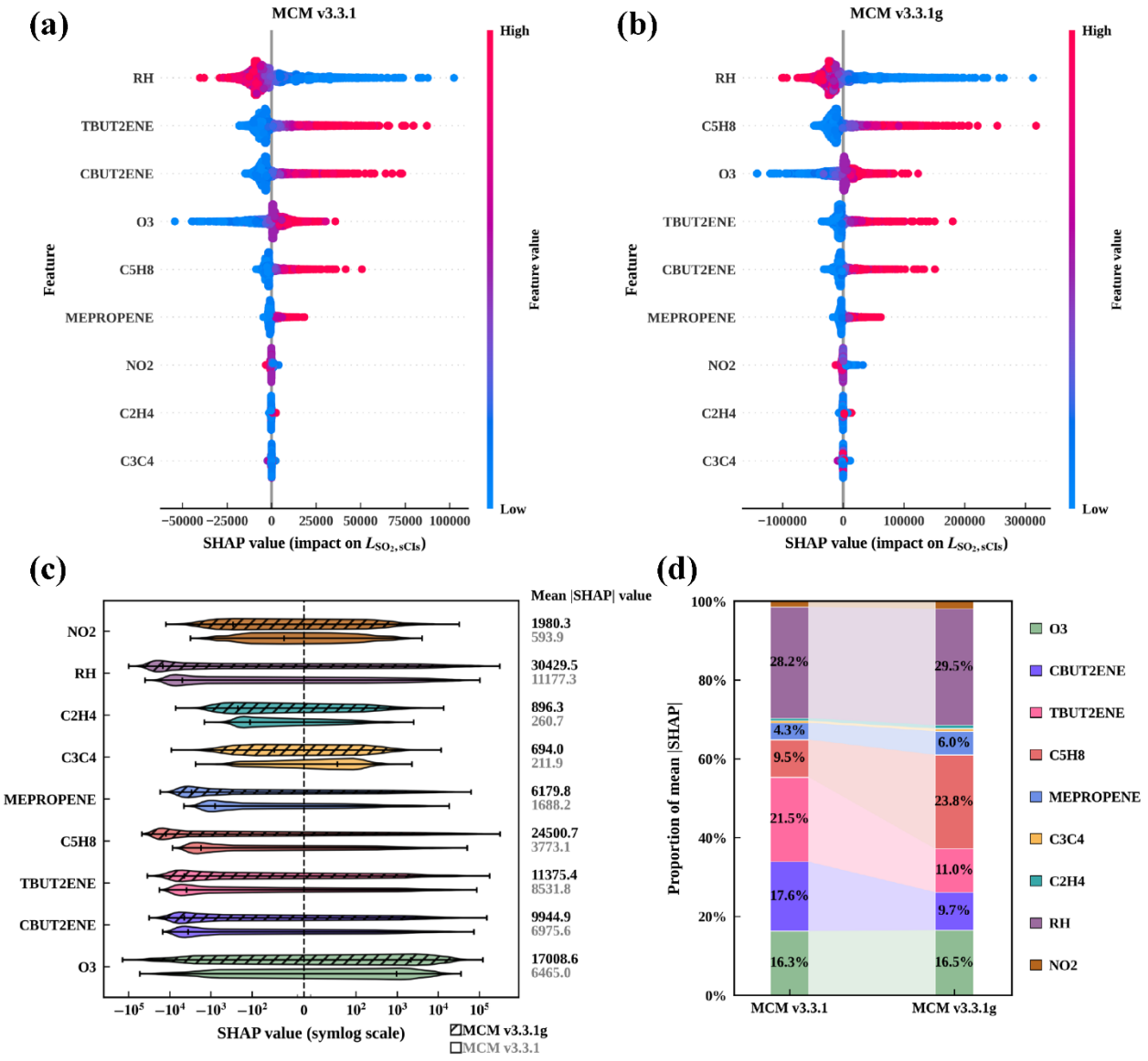

Figure 1. SHAP beeswarm summary plots for the XGBoost surrogate models of $L_{SO2,sCIs}$ under (a) MCM v3.3.1 and (b) MCM v3.3.1g. Each point represents one simulation scenario, positioned according to its SHAP value (molecule·cm^{-3}·s^{-1}) for the corresponding feature. Point colour denotes the feature value from low to high. Features are ordered by mean absolute SHAP value, so that those at the top exert the strongest overall influence on the predicted sCI-driven SO_2 oxidation rate. (c) Comparison of SHAP-value distributions for individual features between the XGBoost surrogate models trained on MCM v3.3.1 and MCM v3.3.1g. Boxplots summarize the full distribution of SHAP values across all simulation scenarios. Differences between mechanism versions reflect how the kinetic update alters both the magnitude of feature effects. (d) Relative feature contributions to the XGBoost surrogate models of $L_{SO2,sCIs}$ under MCM v3.3.1 and MCM v3.3.1g, quantified as the normalized mean absolute SHAP value of each feature. Contributions are expressed as fractions of the total ∑|SHAP| for each model. This comparison highlights how the mechanism update redistributes the overall importance among ozonolysis precursors and competing sinks.

The strengthened interaction effects (Fig. 2) after the update further elucidate the mechanistic origin of these attribution differences. The elevated SHAP interaction values involving RH and both O_3 and alkene indicate that MCM v3.3.1 substantially underestimates the competitive scavenging of sCIs by $H_2O/(H_2O)_2$, thereby masking the strong regulative role of humidity in sCI-mediated SO_2 oxidation. In parallel, interaction effects between O_3 and the individual alkene are also enhanced in MCM v3.3.1g, but with markedly different magnitudes across alkenes. This behaviour is consistent with the update introducing a more realistic representation of sCI structural-specific reactivity: for some alkene systems, like isoprene(C5H8), correcting sCI+SO_2/H_2O kinetics and adding sCI+$(H_2O)_2$ reactions substantially alter the response of $L_{SO2,sCIs}$ to perturbations of alkene and O_3 concentrations. In contrast, other alkene systems, such as CBUT2ENE and TBUT2ENE, exhibit minimal shifts, as the mechanism updates result in comparable scale similarly increases in SO_2 and $H_2O/(H_2O)_2$ scavenging pathways. Overall, these results indicate that simulation biases in MCM v3.3.1 primarily arise from a profound underestimation of sCI+SO_2 and sCI+ $H_2O/(H_2O)_2$ rate coefficients to varying degrees, alongside the omission of loss pathway discrepancies among different sCI species (including stereoisomer-dependent unimolecular decomposition and bimolecular reactions). By rectifying these deficiencies, MCM v3.3.1g provides a more accurate mechanistic description for identifying key precursors and understanding the dependence of their impact on environmental conditions.

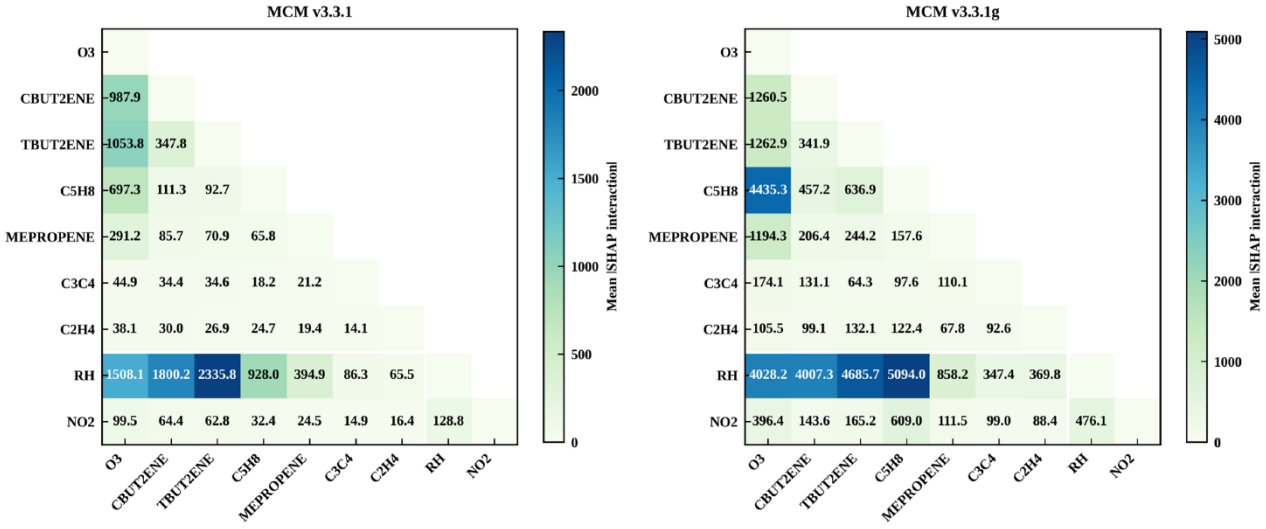

Figure 2. Heat maps of pairwise SHAP interaction strengths among the nine input features for the XGBoost surrogate models of $L_{SO2,sCIs}$ under MCM v3.3.1 and MCM v3.3.1g. Colours denote the mean absolute SHAP interaction value for each feature pair across all simulation scenarios. Larger values indicate stronger non-additive interactions in the surrogate prediction, thereby identifying the combinations of precursors and sinks that most strongly modulate sCI-driven SO_2 oxidation.

Based on the MCM v3.3.1g results, isoprene contributes more than twice as much as cis-/trans-2-butene, 3.8 times as much as isobutene, and roughly thirty times more than ethene and propene/1-butene in terms of their attributed influence on

$L_{SO2,sCIs}$. This ranking demonstrates that alkene importance emerges from the combined influence of ozonolysis kinetics, effective sCI yield (i.e., the fraction of sCIs that persist to undergo bimolecular reactions), and the relative importance of sCI+SO_2 vs. sCI+H_2O/$(H_2O)_2$ pathways. These parameters, which are related to the chemical evolution of sCIs, collectively shape the relationship between alkenes and $L_{SO2,sCIs}$. At 298.15 K, the ozonolysis rate coefficients span more than two orders of magnitude (Table S1), following the order: trans-2-butene (2.0×10^{-16} $cm^3 \cdot molecule^{-1} \cdot s^{-1}$) > cis-2-butene ($1.3 \times 10^{-16}$ $cm^3 \cdot molecule^{-1} \cdot s^{-1}$) > isoprene ($1.28 \times 10^{-17}$ $cm^3 \cdot molecule^{-1} \cdot s^{-1}$) ≈ 2-methylpropene ($1.15 \times 10^{-17}$ $cm^3 \cdot molecule^{-1} \cdot s^{-1}$) ≈ propene ($1.05 \times 10^{-17}$ $cm^3 \cdot molecule^{-1} \cdot s^{-1}$) ≈ 1-butene ($1.00 \times 10^{-17}$ $cm^3 \cdot molecule^{-1} \cdot s^{-1}$) > ethene ($1.56 \times 10^{-18}$ $cm^3 \cdot molecule^{-1} \cdot s^{-1}$). Total sCI yields follow the sequence: isoprene (0.66; 0.55 CH_2OO + 0.08 MVKOO + 0.03 MACROO) > ethene (0.42; CH_2OO) > propene (0.28; 0.20 CH_2OO + 0.08 CH_3CHOO) > 1-butene (0.23; 0.15 CH_2OO + 0.08 C_2H_5CHOO) ≈ trans-2-butene (0.22; CH_3CHOO) ≈ cis-2-butene (0.20; CH_3CHOO) ≈ 2-methylpropene (0.20; 0.13 CH_2OO + 0.07 $(CH_3)_2COO$). Beyond overall yield, sCI speciation varies considerably: aside from cis- and trans-2-butene, CH_2OO is the dominant sCI across all remaining alkene systems. Critically, the bimolecular reactivities of sCIs are strongly structure-dependent. With respect to SO2 oxidation, CH_3CHOO, C_2H_5CHOO, $(CH_3)_2COO$, and MACROO exhibit rate coefficients three to four times higher than those of CH_2OO and MVKOO. The reactivity order toward H_2O/$(H_2O)_2$ is markedly different, however, broadly following CH_3CHOO ≈ C_2H_5CHOO > CH_2OO > MVKOO ≈ $(CH_3)_2COO$ >> MACROO. These contrasts in sCI fate are the fundamental reason why alkene importance cannot be reduced to simple kinetic or yield arguments.

Fig. 3 further shows the effects of various alkenes on $L_{SO2,sCIs}$ at different concentrations under MCM v3.3.1g. Consistent with the average |SHAP| ranking, isoprene, trans-2-butene, cis-2-butene, and 2-methylpropene all exhibit substantially positive impacts as their concentrations increase, whereas ethene and the combined propene/1-butene feature (C3C4) display near-zero or weakly positive dependence across the investigated concentration range. The substantial vertical dispersion at fixed alkene concentrations, observed for all alkenes, indicates that identical alkene abundances can yield markedly different impacts on $L_{SO2,sCIs}$—the signature of non-linear responses due to interactions. For most alkenes (excluding C3C4), this vertical spread increases with concentration, indicating that higher alkene expand the range of $L_{SO2,sCIs}$ while the realized magnitude remains strongly contingent on the ambient environment. Propene/1-butene (C3C4), by contrast, shows large vertical dispersion across the full concentration range without a corresponding concentration dependence, consistent with variability driven almost entirely by interaction effects. And Ethene similarly shows a significant degree of dispersion in its SHAP values at low concentrations. In conclusion, the impact of all alkenes on $L_{SO2,sCIs}$ and their concentrations are not linearly related; however, their nonlinear relationships with $L_{SO2,sCIs}$ vary, meaning that there are differences in the relative strength of interactive effects between different alkenes and other feature variables. The interaction diagnostics in Fig. 2 show that RH has the strongest interaction effect, which motivates the use of RH colouring in Fig. 3 to visualize humidity control. Across all alkenes, higher RH consistently suppresses contributions of alkenes to $L_{SO2,sCIs}$, reflecting enhanced competitive removal of sCIs by H_2O/$(H_2O)_2$. The degree of suppression, however, varies markedly with alkene identity, and can be rationalized directly from the kinetic properties of their produced sCIs. The impact of C3C4 on $L_{SO2,sCIs}$ primarily

stems from their interaction with RH. This is due to the relatively low reaction rates of propene/1-butene and O_3, resulting in significantly lower yields of sCIs compared to C2H4 and C5H8. The primary products of sCIs are CH_2OO, CH_3CHOO, and C_2H_5CHOO, all of which exhibit substantial reactivity with $H_2O/(H_2O)_2$. Additionally, CH_2OO, which constitutes the largest proportion, has relatively low reactivity with SO_2. Consequently, the already insufficiently produced sCIs have even more limited capacity to react with SO_2. Ethene, despite having the slowest ozonolysis rate coefficient, produces CH_2OO with a substantially higher yield (0.42) than propene or 1-butene, partially compensating for its sluggish kinetics. However, since CH_2OO is efficiently scavenged by $H_2O/(H_2O)_2$, ethene's contribution remains small and sensitive to humidity, consistent with the mixed positive and negative SHAP values observed at low concentrations in Fig. 3. In contrast, cis-2-butene and trans-2-butene benefit from both the highest ozonolysis rate coefficients among the investigated alkenes and only production of CH_3CHOO, which reacts rapidly with SO_2. These advantages translate into strong positive contributions to $L_{SO2,sCIs}$; however, because CH_3CHOO is also highly reactive toward $H_2O/(H_2O)_2$, the realized contribution is strongly RH-dependent, as evidenced by the pronounced RH stratification in the dependence plots. 2-Methylpropene generates both CH_2OO and $(CH_3)_2COO$. $(CH_3)_2COO$ reacts rapidly with SO_2 but comparatively slowly with $H_2O/(H_2O)_2$, thereby partially decoupling the SO2 oxidation pathway from humidity competition. This mixed sCIs explains why 2-methylpropene shows a weaker apparent RH interaction and the smallest vertical dispersion growth with concentration among the more influential alkenes—its contribution is more nearly linear because $(CH_3)_2COO$ maintains SO_2 reactivity even under elevated humidity. Isoprene exhibits the strongest positive contribution to $L_{SO2,sCIs}$ across the full humidity range, arising from the favourable combination of relatively fast ozonolysis, the highest total sCI yield (0.66), and a diverse sCIs that includes not only CH_2OO but also MVKOO and MACROO. MACROO rapidly with SO_2 while being slowly with $H_2O/(H_2O)_2$ scavenging, sustaining efficient SO_2 oxidation even at high RH. The interaction between isoprene and RH thus primarily attributed to the CH_2OO fraction, whereas MVKOO and MACROO maintain isoprene to remain a dominant driver of $L_{SO2,sCIs}$ across a wider humidity range. Taken together, when the investigated alkenes are perturbed over comparable concentration ranges, ethene and propene/1-butene exert negligible direct control on $L_{SO2,sCIs}$ relative to the remaining alkenes. Isoprene and the C_4 alkenes—cis-/trans-2-butene and 2-methylpropene—represent the dominant alkene precursors, but their effective impacts are jointly shaped by RH through the competition between SO_2 oxidation and water-driven sCI loss. This finding underscores the necessity of a systematic modeling for decoupling the complex, non-linear atmospheric reactions into a clear precursor-sCI-SO_2 relationship to identify key alkene precursors and quantifying their roles in sCIs-mediated SO_2 oxidation.

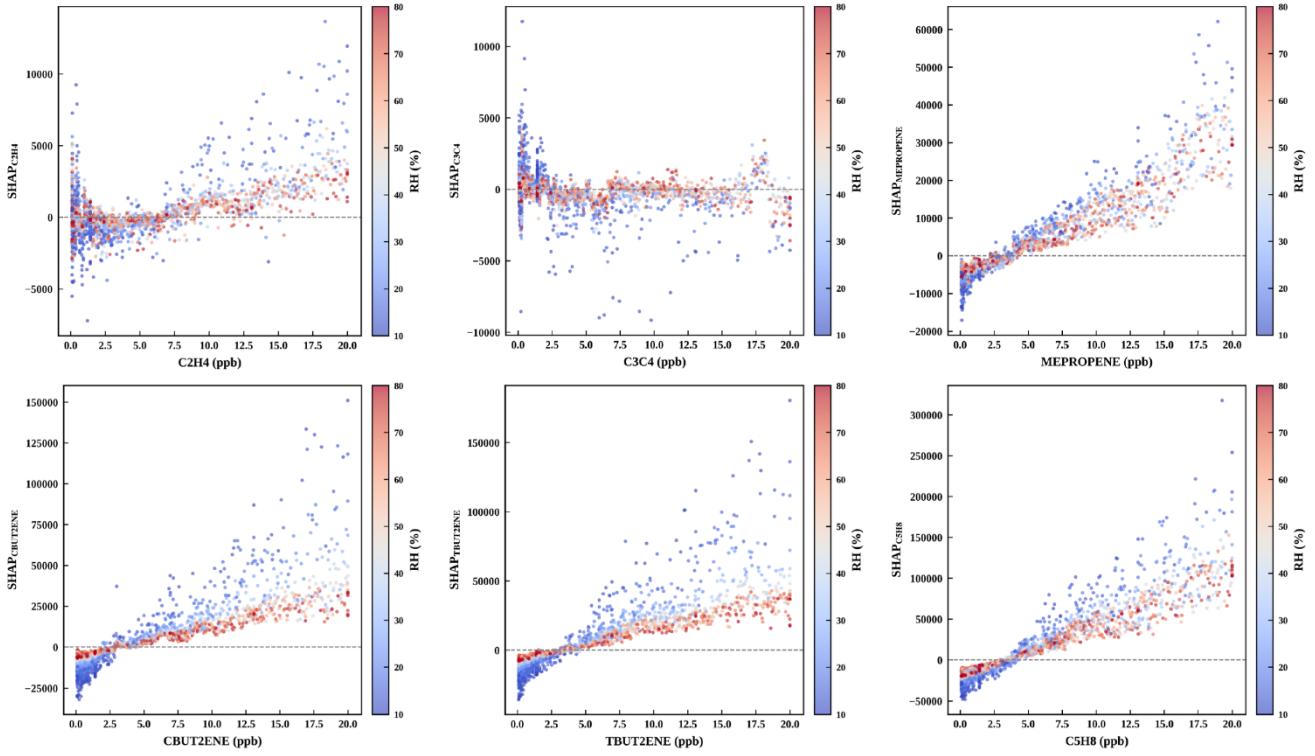

Figure 3. SHAP dependence plots for O_3 and the six alkene precursors in the XGBoost surrogate models of $L_{SO2,sCIs}$. The *x* axis shows the feature value, the *y* axis shows the SHAP value of the same feature, and point colour represents RH. Each point corresponds to one simulation scenario. These plots illustrate both the marginal effect of each alkene precursor on the predicted sCI-driven SO_2 oxidation rate and its interaction with humidity.

3.2 Controls on sCIs contribution and regime-dependent sensitivity of SO_2 oxidation

The surrogate model developed in Sect. 3.1 quantifies how key factors govern $L_{SO2,sCI}$, the absolute rate of SO_2 oxidation by sCIs. A large $L_{SO2,sCI}$, however, does not by itself imply that sCIs are important for SO_2 oxidation, since this depends on the strength of the parallel OH-driven oxidation pathway. OH and sCIs share certain precursors, but their formation pathways are not entirely identical: alkene ozonolysis simultaneously produces both, so alkenes and O_3 drive both pathways, yet OH is additionally sustained through routes that do not involve sCIs, including RO_x–NO_x radical cycling and the direct photolysis of O_3, HONO, and other species. OH is therefore governed by a broader set of factors, including NO_x, NO_2%, and the wider VOC composition, several of which exert little or no direct influence on sCI chemistry. As a result, the two oxidation rates do not respond in tandem to environmental perturbations, such that the relative importance of sCIs shapes the sensitivity of L_{SO2} to its controlling factors. To systematically diagnose under what atmospheric conditions sCIs play a significant role in SO_2 oxidation, and how this role modulates the precursor sensitivity of L_{SO2}, we constructed dedicated surrogate models for μ_{sCI} and L_{SO2}. Their feature sets capture the key controls on both pathways (see Sect. 2.3), and they were trained on a large ensemble of constrained AtChem simulations spanning atmospheric conditions representative of anthropogenically and

biogenically influenced environments. Because photolysis exerts decisive control over OH production, daytime (08:00–18:00 CST) and nighttime (22:00–05:00 CST) conditions were treated as separate analyses.

Sobol sensitivity analysis was applied to identify the dominant atmospheric controls on μ_{sCIs} and to quantify the extent to which each feature exerts its influence independently or through interactions with other features for the daytime period (Fig. 4a). Here, the first-order index S_1 measures the independent main-effect contribution of a single feature, whereas the total-order index S_T additionally encompasses all higher-order interactions involving that feature; a markedly larger S_T relative to S_1 therefore signals that a feature operates predominantly through coupling with other features rather than through its own variation alone. The analysis identifies ARI, O_3, alkene%, and VOCs as the dominant controls on μ_{sCIs}, with independent contributions ranked as ARI (S_1 = 0.18) > O_3 (S_1 = 0.16) > alkene% (S_1 = 0.15) > VOCs (S_1 = 0.11). RH ranks immediately behind (S_1 = 0.09), while NO_x and NO_2% register the weakest direct contributions (S_1 = 0.05 and 0.03, respectively). The low-ARI tier (ARI = 0) is dominated by ethene and propene, representative of typical urban anthropogenic emissions; the mid-ARI tier (ARI = 1) features an elevated proportion of 2-butenes, characteristic of industrial source environments such as rubber manufacturing; and the high-ARI tier (ARI = 2) is driven primarily by isoprene, representative of biogenic or petrochemical-influenced conditions. The mixture proportions of the alkenes at each ARI level are detailed in Fig. S1. Comparing S_1 and S_T across all features reveals a clear differentiation in how each feature exerts its influence. For RH, $S_T \approx S_1$ (S_T = 0.11), indicating negligible interaction effects; RH influences μ_{sCIs} almost entirely through its independent main effect. For ARI, O_3, alkene%, and VOCs, S_T substantially exceeds S_1, indicating that although their independent main effects dominate, significant interaction effects are also present. Among these, ARI exhibits both the largest S_1 and S_T, reinforcing that alkene speciation not only exerts the strongest independent control on μ_{sCIs} but also acts as a key moderator of the effects of O_3, alkene%, and VOCs. The contrast is most pronounced for NO_x and NO_2%: their S_1 values account for less than half of their respective S_T values (NO_x: S_T = 0.12; NO_2%: S_T = 0.08), indicating that their influence on μ_{sCIs} is overwhelmingly mediated through interactions with other features rather than through direct action. This strong interaction dependence reflects the fact that their influence on μ_{sCIs} is conditional on the values of other features.

The directional effect of these features are further elucidated by the two-dimensional partial dependence plots (2D-PDPs; Fig. 4b-i). Among the features that directly govern $L_{SO2,sCI}$, ARI, O_3, VOCs, and alkene% exhibit mutually reinforcing positive effects on μ_{sCIs}, suggesting that conditions favorable for alkene ozonolysis simultaneously enhance the relative competitiveness of the sCI pathway. RH exerts a negative effect on μ_{sCIs}, suppressing the sCI+SO_2 pathway via $H_2O/(H_2O)_2$ losses. Despite NO_2 being a known sCIs scavenger, NO_2% exhibits a synergistic co-enhancement with O_3 and VOCs on μ_{sCIs}. These synergistic effects are expected to arise from the influence of NO_2% on OH, through its role in governing how NO_x is partitioned between radicals termination and cycling. A higher NO_2 fraction, at fixed total NO_x, is expected to reduce the NO available for $HO_2/RO_2 \rightarrow OH$ conversion, thereby suppressing the SO_2+OH oxidation channel more strongly than it scavenges sCIs, particularly under high-O_3 and high-alkene% conditions. Correspondingly, the greater the NO_2%, the more strongly μ_{sCIs} increase with rising O_3, VOCs, and alkene%. NO_x, by contrast, exerts predominantly suppressive interactions with O_3 and VOCs: μ_{sCIs} peak at the lowest NO_x levels and decline sharply as NO_x increases only slightly from its minimum,

before levelling off or increasing slightly at higher concentrations. The sensitivity of O_3, alkene%, and VOCs on μ_{sCIs} is modulated by NO_x levels: at near-zero level, increases in O_3 and VOCs produce the largest increments in μ_{sCIs}; across the remainder of the NO_x level range, the increase in μ_{sCIs} driven by rising O_3 and VOCs from their lowest to highest levels falls within 0.03–0.04. The effect of NO_x on μ_{sCIs} arises primarily from its control over the steady-state OH concentration: at extremely low NO_x level, the radical recycling efficiency is greatly diminished, leading to suppressed OH. Meanwhile, excessively high NO_x level also suppresses OH by accelerating termination reactions between radicals and NO_x. Under both conditions, the attenuation of OH-mediated SO_2 oxidation transfers a greater share of the total oxidation burden to sCIs, resulting in elevated μ_{sCIs}.

Taken together, daytime μ_{sCIs} tends to be elevated under atmospheric conditions characterized by high O_3 concentrations, abundant VOCs, a large alkene fraction, and either near-zero or elevated NO_x levels, combined with relatively low RH. This finding is consistent with previous studies reporting that sCI chemistry plays a more prominent role in SO_2 oxidation in forested and rural environments than in polluted urban settings (Kim et al., 2015). Among the identified controls, O_3, VOCs, alkene%, and ARI, which collectively serve as proxies for sCI precursor abundance, not only directly promote $L_{SO2,sCI}$ but also exhibit pronounced synergistic positive effects on μ_{sCIs}. This pattern implies that as these variables increase, the concurrent enhancement of OH is disproportionately smaller than the gain in sCI production, or may even be moderately suppressed. Consequently, although O_3 and alkene serve as common precursors to both OH and sCIs, the magnitude and direction of their effects on each pathway are not equivalent. Under most daytime conditions, the OH pathway dominates SO_2 oxidation, such that the sensitivity of L_{SO2} to precursor species is primarily shaped by how those precursors affect OH. However, as shown by the NO_x dependence of μ_{sCIs}, the response of OH to precursor perturbations is itself condition-dependent, exhibiting a non-monotonic relationship with NO_x. This gives rise to distinct OH response patterns under high- and low-μ_{sCIs} conditions, and by extension, distinct sensitivities of L_{SO2} to its precursors. To quantify the magnitude of these differences, the dataset was partitioned into high- and low-μ_{sCIs} subsets based on the median daytime μ_{sCIs} value (1.1%), and the relationship between each feature and L_{SO2} was characterised separately for each subset.

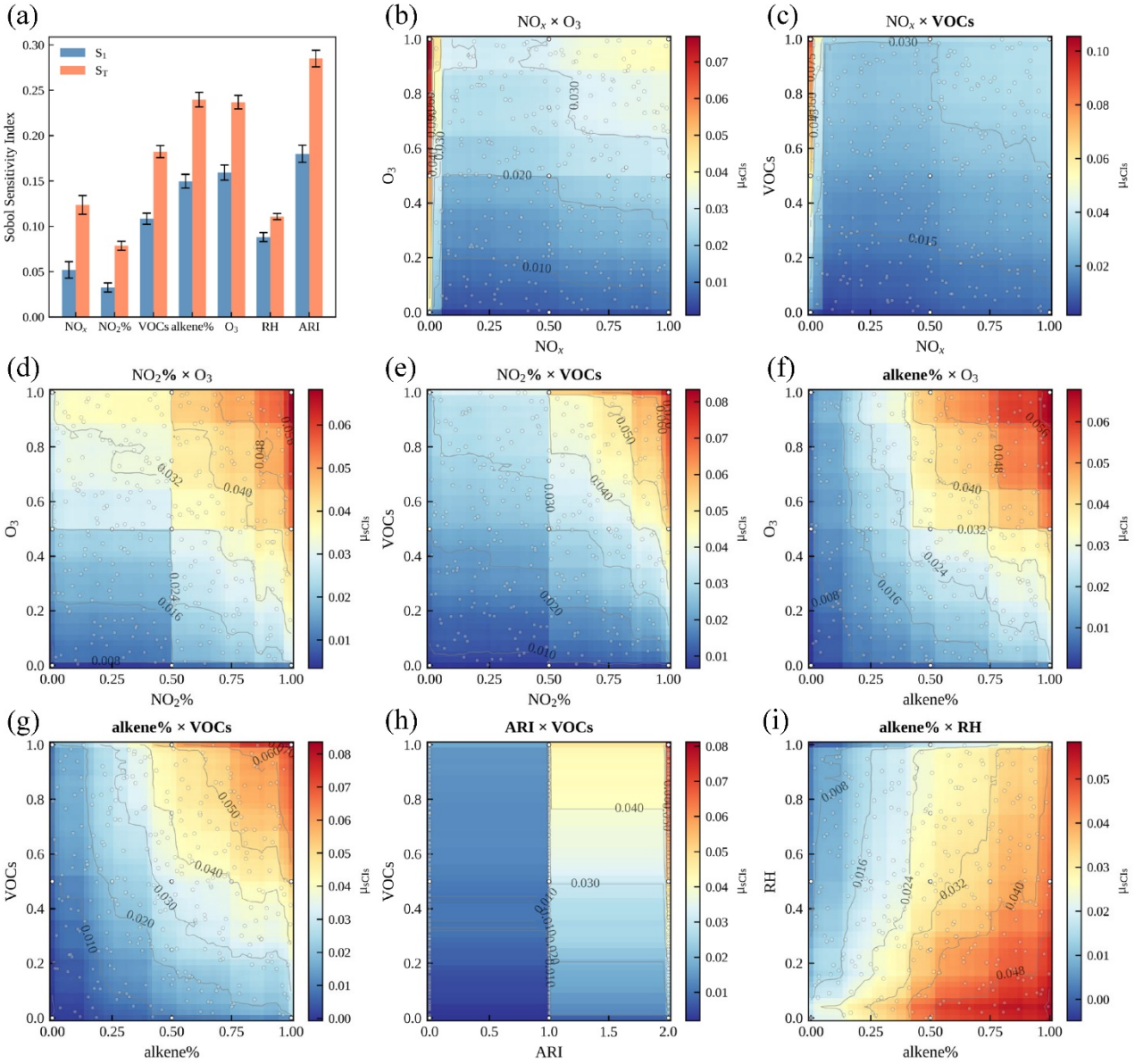

Figure 4. (a) First-order (S_1) and total-order (S_T) Sobol sensitivity indices for the seven input features in the XGBoost surrogate model of μ_{sCIs} during daytime. S_1 quantifies the main effect of each feature acting alone, whereas S_T includes both the main effect and all interaction effects involving that feature. The difference between S_T and S_1 therefore reflects the extent to which a feature participates in non-additive interactions. (b-i) Two-dimensional partial dependence plot showing the joint effect of O_{3norm}×NO_xnorm, VOCsnorm×NO_xnorm, O_3norm×NO_2%norm, VOCsnorm×NO_2%norm, O_3norm×alkene%norm, VOCsnorm×alkene%norm, VOCsnorm×ARIcode, and RHnorm×alkene%norm on the surrogate-model prediction of μ_{sCIs} during daytime. The surface represents the average model response after marginalizing over the remaining features. Warmer colours indicate larger predicted μ_{sCIs}.

Figure 5a illustrates how total gas-phase SO_2 oxidation rate (L_{SO2}) varies with O_3, VOCs, and alkene% across high- and low-μ_{sCIs} regimes. The mean ICE curves show that L_{SO2} increases monotonically with all three precursors under both regimes;

however, the response is systematically enhanced under high-μ_{sCIs} conditions, with the mean curve exhibiting a steeper and more sustained increase across the full feature range. Beyond the mean response, the spread of individual ICE curves provides insight into response heterogeneity, that is, the degree to which the effect of precursors on L_{SO2} varies across different atmospheric conditions. Notably, negative L_{SO2} responses to increases in VOCs and alkene% are observed under extremely low NO_x level. To quantify this directional heterogeneity, we computed the fraction of individual ICE curves that exhibit a net negative slope from the minimum to the maximum feature value (neg-slope fraction). For O_3, near-universal positive associations with L_{SO2} are observed in both regimes, with a neg-slope fraction of 0% under high-μ_{sCIs} and 3% under low-μ_{sCIs} regimes. For alkene%, the neg-slope fraction increases from 8% under high-μ_{sCIs} to 19% under low-μ_{sCIs}. For VOCs, a similar pattern is evident, with the neg-slope fraction rising from 22% under high-μ_{sCIs} to 30% under low-μ_{sCIs} regimes.

This regime contrast warrants further examination. Under extremely low NO_x level, high μ_{sCIs} is associated with abundant alkene concentrations. Although higher alkene loadings promote radical termination reactions, which would be expected to suppress OH and thereby reduce L_{SO2}, the high-μ_{sCIs} subset paradoxically shows a smaller neg-slope fraction than the low-μ_{sCIs} subset. This is expect to suggest that the alkene ozonolysis pathway offsets part of the OH suppression caused by enhanced radical termination, thereby dampening the negative L_{SO2} response. At moderate to high NO_x levels, positive L_{SO2} responses to increases in VOCs, alkene%, and O_3 dominate and are considerably stronger in the high-μ_{sCIs} regime than in the low-μ_{sCIs} regime. This amplified sensitivity likely reflects the fact that high-μ_{sCIs} regime associated with abundant alkenes, which simultaneously promote OH propagation through the RO_x cycling pathway and alkene ozonolysis.

In summary, L_{SO2} exhibits both positive and negative responses to VOCs and alkene% across the full scenario space. The key distinction is that in the high-μ_{sCIs} regime, negative responses are less frequent and positive responses are stronger. To clarify the mechanistic basis of this contrast, specifically why negative L_{SO2} responses to VOCs and alkene% reductions are more frequent in the low-μ_{sCIs} regime, we examine the OH and sCI budgets for two representative scenarios at normalised NO_x levels of 0 and 0.5 (Figs. 5b, 5c). OH production is partitioned into initiation ($\sum OH_{new}$), which encompasses all primary OH production via photolysis and alkene ozonolysis (Sheehy et al., 2010), and propagation (OH_{propag}), defined as the rate of $HO_2 \rightarrow OH$ conversion. Under extremely low NO_x ($NO_{x,\,norm} = 0$), the ozonolysis pathway accounts for 39.65% of $\sum OH_{new}$, and the ratio $OH_{propag}/\sum OH_{new}$ is 3.67, indicating that radical propagation contributes approximately 3.7 times the primary OH production. Under moderate NO_x level ($NO_{x,\,norm} = 0.5$), the ozonolysis share of $\sum OH_{new}$ decreases to 29.28%, while the $OH_{propag}/\sum OH_{new}$ ratio rises to 6.96, reflecting greatly enhanced radical cycling efficiency, as evidenced by the $HO_2 \rightarrow OH$ pathway rate reaching 7.04×10^8 molecules$\cdot$cm$^{-3}\cdot$s^{-1}. At extremely low NO_x level, the RO_x recycling chain is severely suppressed, so primary OH initiation contributes a larger relative fraction to the total OH budget, and the ozonolysis pathway represents a correspondingly larger share of OH production. Under this condition, the contribution of alkene ozonolysis to OH production can effectively counteract the suppressive effect of enhanced radical termination on OH, explaining why the neg-slope fraction for L_{SO2} is reduced in the high-μ_{sCIs} subset relative to the low-μ_{sCIs} subset. At moderate NO_x level, OH is sustained predominantly through cycling rather than through photolysis or ozonolysis, and increased NO_x additionally enhances HONO photolysis, further diminishing the relative contribution of ozonolysis to OH generation. Under these

conditions, perturbations in VOCs and alkene% exert their influence on L_{SO_2} primarily through modulation of OH propagation. Because high-μ_{sCIs} conditions at this NO_x level are associated with abundant alkenes, both the RO_x cycling and ozonolysis pathways are strongly activated, and L_{SO_2} therefore exhibits a pronounced positive response to precursor increases.

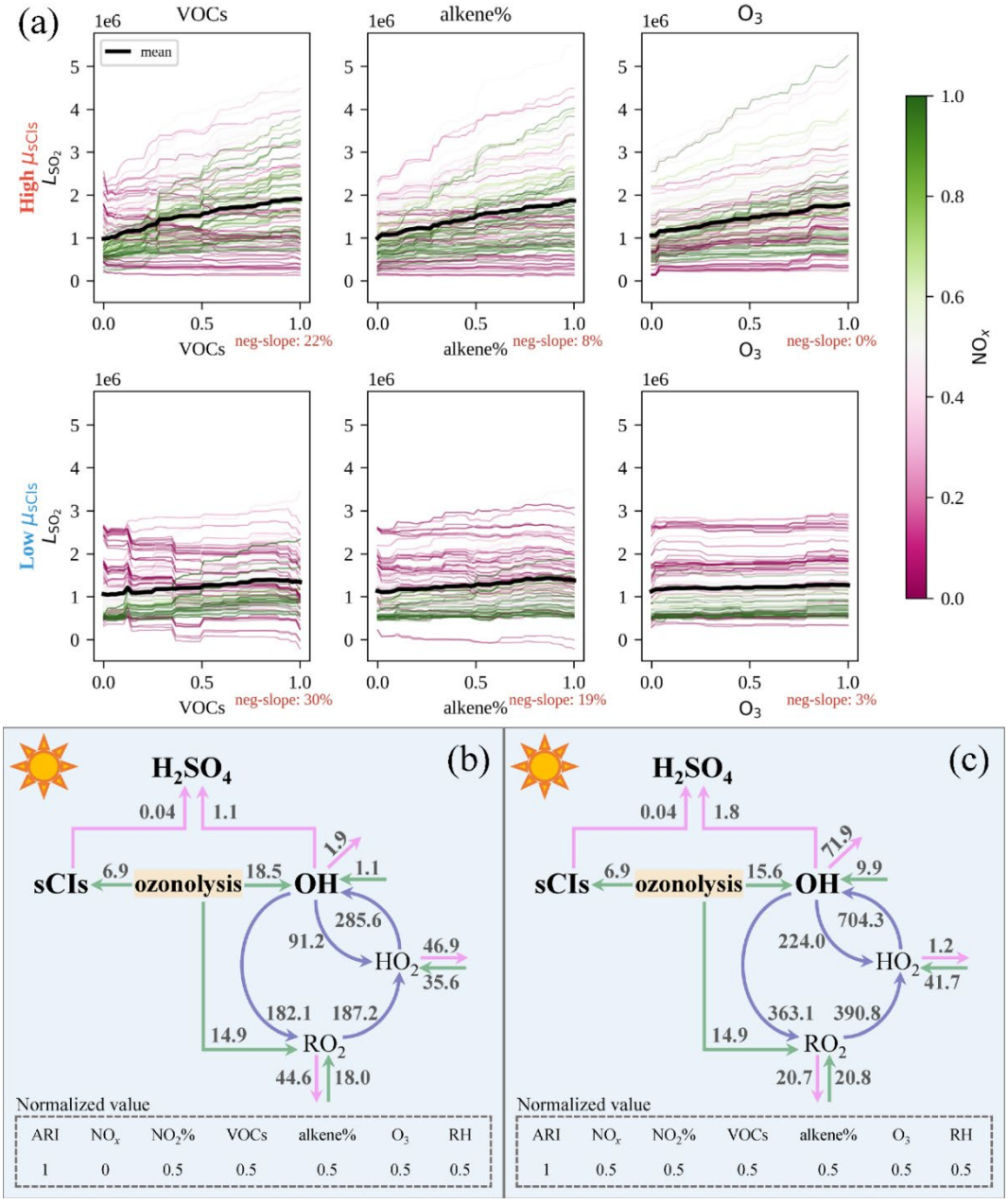

Figure 5. (a) Individual conditional expectation (ICE) plots for the regime-specific L_{SO_2} models during daytime, showing the responses of predicted total gas-phase SO_2 oxidation loss to VOCsnorm, alkene%norm, and O3norm in the low- and high-μ_{sCIs}

regimes. The two rows correspond to the two μ_{sCIs} regimes, and the three columns correspond to the three selected predictors. Each thin curve represents one sampled scenario, coloured by normalized NO_x. The curves are shown in absolute prediction space (i.e. without centering), so both slope and vertical spread reflect heterogeneity in conditional model responses under different chemical backgrounds. (b-c) Two representative daytime scenarios illustrating the budgets of OH and sCIs. Numbers denote reaction rates (10^6 molecules·cm^{-3}·s^{-1}). Pink, green, and purple lines indicate the termination, initiation, and propagation pathways of OH and sCIs, respectively.

The nighttime Sobol sensitivity indices (Fig. 6a) reveal controls on μ_{sCIs} that differ markedly from those identified during the day. ARI, RH and NO_x emerge as the dominant controls, with independent contributions ranked as ARI ($S_1 = 0.23$) > RH ($S_1 = 0.19$) > NO_x ($S_1 = 0.18$). VOCs ($S_1 = 0.13$), alkene% ($S_1 = 0.11$) and O_3 ($S_1 = 0.08$) rank immediately behind, while NO_2% exerts exerting a negligible direct influence ($S_1 = 0.002$). Comparing S_1 and S_T across all features, S_T only slightly exceeds S_1 for most features, indicating that independent main effects dominate and interaction effects are limited, with the total-order ranking following ARI ($S_T = 0.27$) > RH ($S_T = 0.22$) > NO_x ($S_T = 0.21$) > VOCs ($S_T = 0.16$) > alkene% ($S_T = 0.13$) > O_3 ($S_T = 0.10$). NO_2% retains the smallest S_T ($S_T = 0.01$), reinforcing that its regulatory effect on μ_{sCIs} at night is negligible. The close agreement between S_T and S_1 across most features at night stands in sharp contrast to the daytime results, where S_T substantially exceeded S_1 for several key features. This collapse of interaction effects reflects a fundamental mechanistic shift: in the absence of photolysis, the primary OH initiation pathway is alkene ozonolysis, which is simultaneously the sole sCI formation pathway. Perturbations to precursors therefore affect both oxidation pathways in the same direction and with similar magnitude, suppressing the conditional interactions that characterise the daytime sensitivity structure. This finding is broadly consistent with previous studies demonstrating that Criegee intermediate chemistry constitutes a non-negligible OH source under dark or low-light conditions (Khan et al., 2018). The rise of RH from a minor factor during the day to the second-ranked control at night reflects the substantially lower OH concentrations characteristic of nocturnal conditions, which elevate the relative contribution of sCIs to gas-phase SO_2 oxidation (Kukui et al., 2021b) and thereby amplify the suppressive impact of H_2O and $(H_2O)_2$ on μ_{sCIs}. The contrasting behaviour of NO_x and NO_2% between day and night also warrants attention. At night, photolytic regeneration of NO from NO_2 is effectively absent; NO within NO_x is instead oxidised to NO_2 through reactions with O_3 and peroxy radicals, leading to progressive NO_2 accumulation. This enhances the termination reaction between NO_2 and OH, suppressing steady-state OH and indirectly elevating μ_{sCIs}. As a result, nighttime μ_{sCIs} is governed primarily by total NOx abundance rather than by the NO/NO_2 partitioning. This explains why NO_2% exerts a negligible effect at night.

The directional effects of these features are further elucidated by the 2D-PDPs (Figs. 6b-i). ARI, O_3, VOCs, and alkene% exhibit mutually reinforcing positive effects on μ_{sCIs}, consistent with their roles as sCI precursors: conditions favourable for $L_{SO2,sCI}$ simultaneously enhance the relative competitiveness of the sCI oxidation pathway. RH exerts a pronounced negative effect on μ_{sCIs} by suppressing the sCI+SO_2 pathway via H_2O and $(H_2O)_2$ losses. With respect to NO_x, μsCIs reaches its highest value (~0.1) at the lowest NO_x level, then drops sharply as NO_x increases only slightly from its minimum, before

rising significantly and monotonically across the remainder of the concentration range, such that a strong positive relationship between NO_x and μ_{sCIs} prevails across most of the NO_x range. This near-monotonic behaviour reflects the role of NO_x in modulating steady-state OH through radical termination, as described above.

Taken together, nighttime μ_{sCIs} tends to be elevated under atmospheric conditions characterised by high O_3 concentrations, abundant VOCs, a large alkene fraction, and either near-zero or elevated NO_x levels, combined with relatively low RH. This is consistent with previous study reporting that elevated NO_x levels in power plant environments at night are highly conducive to a large sCI contribution fraction (Meidan et al., 2019). Furthermore, ARI, O_3, VOCs, and alkene%, which serve as proxies for sCI precursor abundance, not only significantly promote $L_{SO2,sCI}$ but also exert a pronounced synergistic effect on μ_{sCIs}, indicating that O_3 and alkenes as common precursors to both OH and sCIs do not drive perturbations in these two pathways with the same magnitude or direction at night. Notably, unlike during the day when the OH pathway almost exclusively dominates SO_2 oxidation, the relative contribution of sCIs at night is substantially larger. Meanwhile, the response of OH to precursor perturbations becomes much less condition-dependent. Consequently, the sensitivity of L_{SO2} to its precursors is expected to diverge more substantially across different μ_{sCIs} levels. To quantify this divergence, the dataset was partitioned into high- and low-μ_{sCIs} subsets based on the median nighttime μ_{sCIs} value (8.0%), and the relationship between each feature and L_{SO2} was characterised separately for each subset.

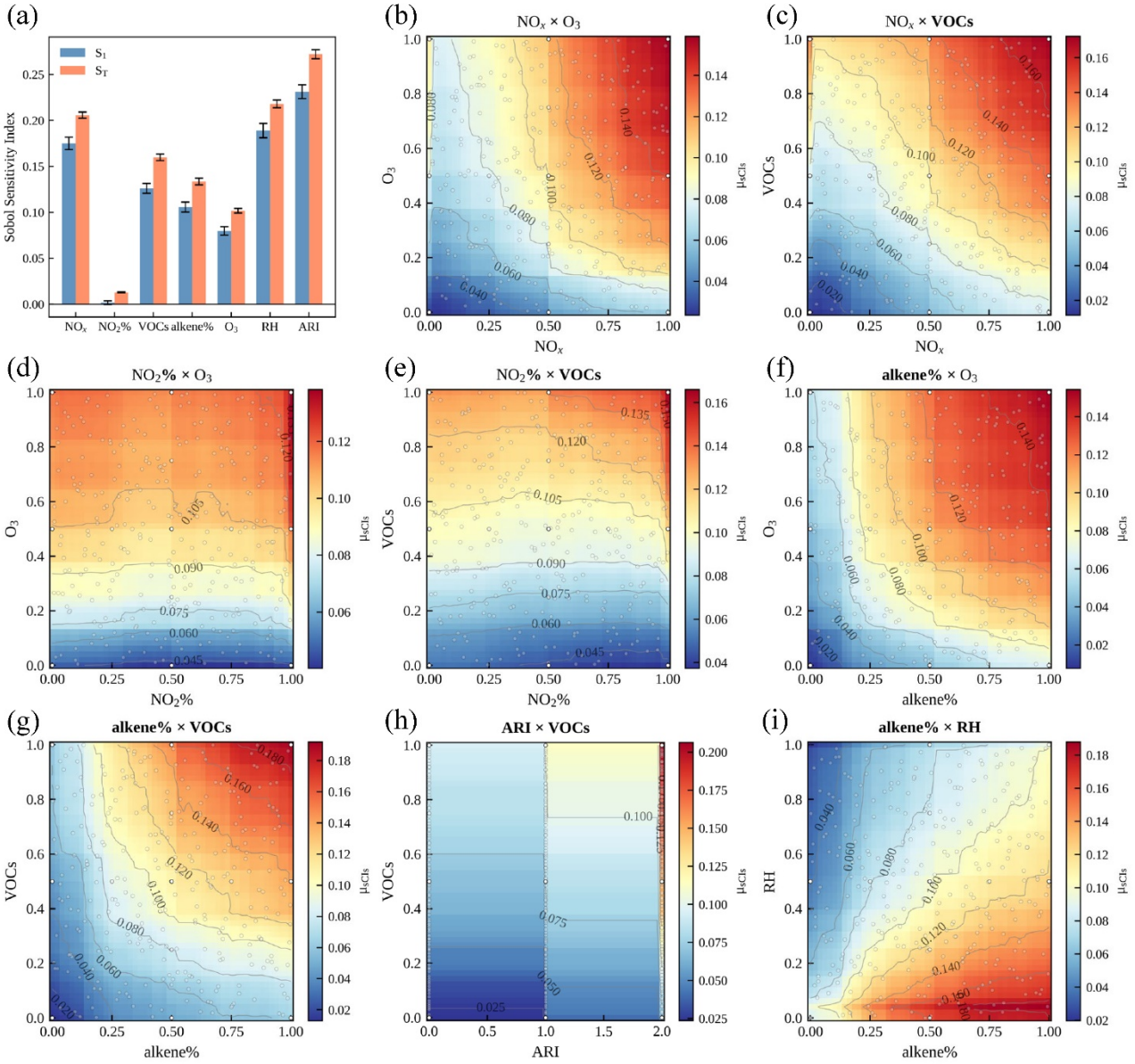

Figure 6. (a) First-order (S_1) and total-order (S_T) Sobol sensitivity indices for the seven input features in the XGBoost surrogate model of μ_{sCIs} during nighttime. S_1 quantifies the main effect of each feature acting alone, whereas S_T includes both the main effect and all interaction effects involving that feature. The difference between S_T and S_1 therefore reflects the extent to which a feature participates in non-additive interactions. (b-i) Two-dimensional partial dependence plot showing the joint effect of O_{3norm}×NO_xnorm, VOCsnorm×NO_xnorm, O_3norm×NO_2%norm, VOCsnorm×NO_2%norm, O_3norm×alkene%norm, VOCsnorm×alkene%norm, VOCsnorm×ARIcode, and RHnorm×alkene%norm on the surrogate-model prediction of μ_{sCIs} during nighttime. The surface represents the average model response after marginalizing over the remaining features. Warmer colours indicate larger predicted μ_{sCIs}.

Figure 7a show how total gas-phase SO_2 oxidation (L_{SO2}) responds to precursor perturbations across high-μ_{sCIs} and low-μ_{sCIs} regimes during nighttime. The mean ICE curves reveal that L_{SO2} increases monotonically with all three precursors under both

regimes; however, the response is systematically enhanced under high-μ_{sCIs} regime, with the mean curve exhibiting a steeper and more sustained increase across the full feature range. Beyond the mean response, the spread of individual ICE curves provides insight into response heterogeneity across different atmospheric conditions. For O_3, near-universal positive associations with L_{SO2} are observed in both regimes, with neg-slope fraction of 0% and 1% under high- and low-μ_{sCIs} conditions, respectively, indicating that O_3 consistently promotes L_{SO2} regardless of the sCI regime. For alkene%, the neg-slope fraction increases from 3% under high-μ_{sCIs} to 5% under low-μ_{sCIs} conditions. The contrast is most pronounced for VOCs, where the neg-slope fraction rises from 6% under high-μ_{sCIs} to 31% under low-μ_{sCIs} regime, with the excess negative responses in the low-μ_{sCIs} regime arising predominantly from high-NO_x scenarios. To elucidate the role of the alkene ozonolysis pathway in driving these response differences, we examine the OH and sCI budgets for two representative scenarios at high NO_x level, corresponding to low-μ_{sCIs} (μ_{sCIs} = 0.008) and high-μ_{sCIs} (μ_{sCIs} = 0.14) regimes, respectively (Figs. 7b, 7c).

Under the low-μ_{sCIs} regime (μ_{sCIs} = 0.008), the ozonolysis pathway accounts for only 4.35% of $\sum OH_{new}$, with $\sum OH_{new}$ of 3.86 × 10^6 molecules·cm^{-3}·s^{-1}. Under the high-μ_{sCIs} regime (μ_{sCIs} = 0.14), the ozonolysis pathway contributes 94.24% of $\sum OH_{new}$, with $\sum OH_{new}$ of 2.29 × 10^7 molecules·cm^{-3}·s^{-1}. These results confirm that the ozonolysis pathway is not only the formation pathway for sCIs but also the primary OH initiation pathway under conditions where alkenes or O_3 are abundant at night. When the ozonolysis pathway is weak, primary OH production is limited to a residual photolysis source in the early morning hours, and OH is sustained predominantly through its cycling with the non-alkene VOC pool via OH→RO_2/HO_2 reactions. Under these conditions, a reduction in total VOC suppresses the OH→RO_2/HO_2 sink, lengthening radical lifetime and raising steady-state OH and $L_{SO2,OH}$. Because the alkene-derived sCI flux is negligible in this regime, $\Delta L_{SO2,sCI} \approx 0$, and the OH rebound effect dominates, resulting in a net increase in L_{SO2} upon VOC reduction (negative slope). Conversely, when the ozonolysis pathway is strong, it simultaneously serves as the primary OH initiation source and the dominant sCI formation pathway. Under these conditions, VOC perturbations affect both oxidation pathways in the same direction, substantially reducing the occurrence of negative L_{SO2} responses. Comparing the two scenarios, the ozonolysis→sCIs and ozonolysis→OH rates increase by factors of 127.5 and 123.3, respectively, while the sCIs→H_2SO_4 rate increases by a factor of 133 compared to only 6-fold for OH→H_2SO_4. This asymmetry arises because OH also reacts with alkenes and participates in a residual radical cycle at night, partially decoupling OH concentration from the ozonolysis rate. The contrasting neg-slope fractions for VOCs versus alkene% can be understood by recognizing that reducing alkene% simultaneously withdraws a primary OH initiation source and the sCI formation pathway, so L_{SO2} almost universally declines (neg-slope ≤ 5%). In contrast, reducing total VOC perturbs primarily the OH sink rather than the OH source; under alkene-poor (low-μ_{sCIs}) conditions, this can trigger an OH rebound that outweighs the negligible change in the sCI pathway, producing a negative L_{SO2} response (neg-slope = 31%).

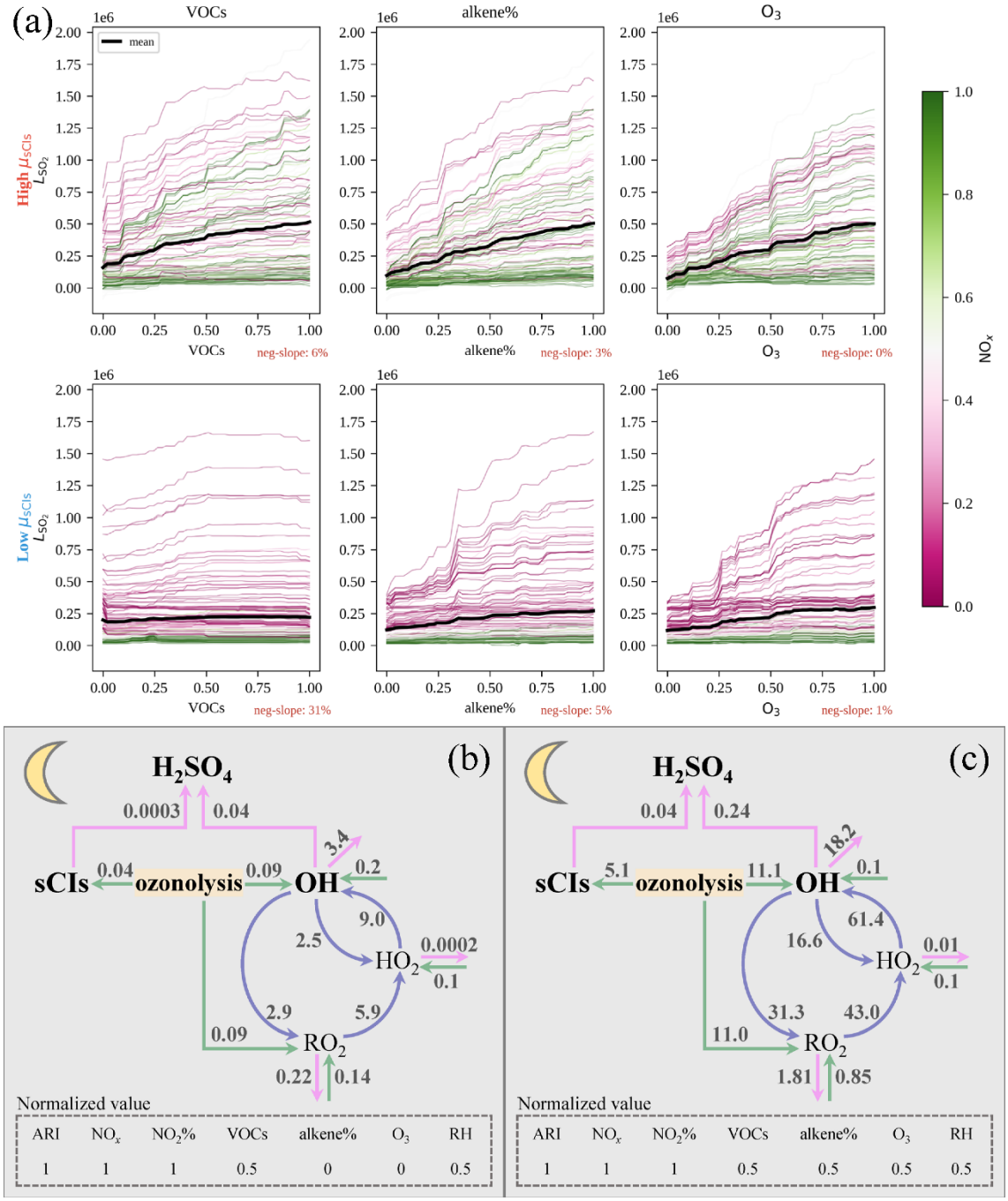

677

678 **Figure 7. (a) Individual conditional expectation (ICE) plots for the regime-specific L_{SO2} models during nighttime, showing the**
679 **responses of predicted total gas-phase SO_2 oxidation loss to VOCsnorm, alkene%norm, and O_3norm in the low- and high-μ_{sCIs}**
680 **regimes. The two rows correspond to the two μ_{sCIs} regimes, and the three columns correspond to the three selected predictors.**
681 **Each thin curve represents one sampled scenario, coloured by normalized NO_x. The curves are shown in absolute prediction space**

(i.e. without centering), so both slope and vertical spread reflect heterogeneity in conditional model responses under different chemical backgrounds. (b-c) Two representative nighttime scenarios illustrating the budgets of OH and sCIs. Numbers denote reaction rates (10^6 molecules·cm^{-3}·s^{-1}). Pink, green, and purple lines indicate the termination, initiation, and propagation pathways of OH and sCIs, respectively.

3.3 Observational–model corroboration of the μ_{sCIs} regime-dependent sensitivity of SO_2 oxidation

To validate the predictive capability of the surrogate model developed in Section 3.2 for μ_{sCIs}, and to evaluate the dependence of SO_2 oxidation sensitivity to its precursors on sCIs contributions in ambient air, we selected a summer episode in Wuhai City as a real-atmosphere validation testbed. Figure 8 presents the constrained simulation results derived from AtChem-MCM v3.3.1, including time series of sulfuric acid concentrations (H_2SO_4-AtChem) and the fractional contribution of sCIs to total SO_2 oxidation (μ_{sCIs}-AtChem) over the period 1 June–15 July 2021. SO_4^{2-} denotes the ambient particulate sulfate mass concentrations measured concurrently by online ion chromatography. The terms "μ_{sCIs}-surrogate model" represent the daytime- and nighttime-averaged μ_{sCIs} predictions generated by the surrogate model described in Section 3.2. The strong agreement (R^2 = 0.75) between the surrogate predictions (μ_{sCIs}-surrogate model) and the explicit AtChem simulations (μ_{sCIs}-AtChem) demonstrates the robust predictive performance of the constructed machine learning surrogate for μ_{sCIs}.

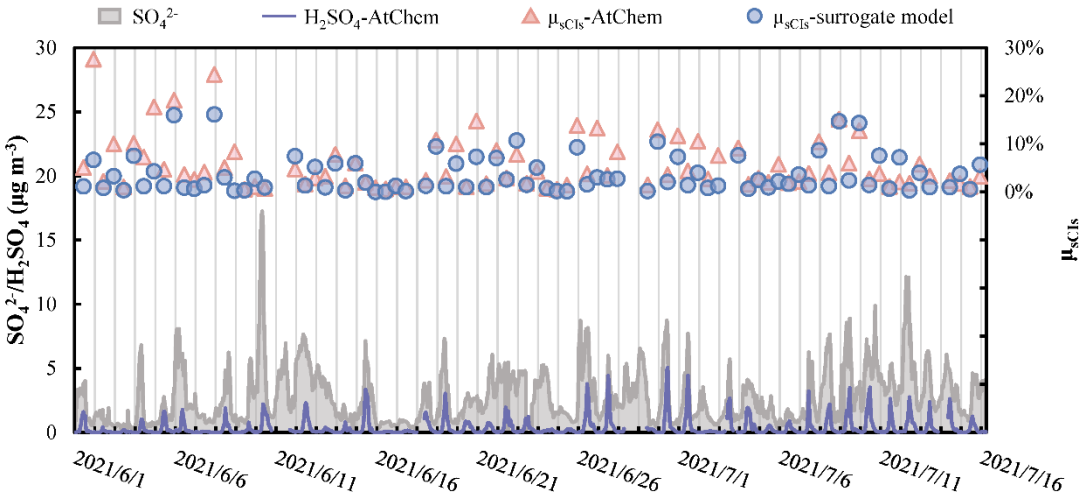

Figure 8. Constrained AtChem–MCM v3.3.1 simulations for a summer episode in Wuhai City (1 June–15 July 2021), showing time series of H_2SO_4-AtChem (AtChem-simulated sulfuric acid concentration), μ_{sCIs}-AtChem (AtChem-simulated fractional contribution of sCIs to total SO_2 oxidation), SO_4^{2-} (concurrently measured ambient particulate sulfate mass concentration), and μ_{sCIs}-surrogate model (daytime- and nighttime-averaged μ_{sCIs} predicted by the surrogate model).

To evaluate whether ambient SO_4^{2-} concentrations serve as a reliable proxy for gas-phase H_2SO_4 production during the target period, an XGBoost model was trained on a comprehensive long-term observational dataset spanning 9 October 2019 to 30 June 2022 (summary statistics of all variables are provided in Table S4), with hourly SO_4^{2-} concentration as the target

variable. The feature set included $PM_{2.5}$, NO_3^-, SO_2, O_3, VOCs, alkene%, NO_x, NO_2%, RH, wind speed (WS), and Fe. Training over this extended period ensures that the model captures the full range of variability in sulfate formation, spanning seasonal cycles, episodic pollution events, and varying meteorological regimes, thereby establishing a representative and well-generalised mapping between precursor conditions and SO_4^{2-}. SHAP values were then extracted exclusively for the target episode (1 June–15 July 2021) to attribute feature contributions during this specific period.

As shown in Figure 9a, the three highest-ranked features are NO_3^-, SO_2, and $PM_{2.5}$, all of which exhibit clear positive correlations with SO_4^{2-}. The dominant role of NO_3^- is consistent with the co-accumulation of secondary inorganic aerosols (Gao et al., 2021): elevated NO_3^- co-occurs with SO_4^{2-} during secondary aerosol formation episodes, collectively driving increases in $PM_{2.5}$. The strong positive SHAP contribution of SO_2 directly corroborates its role as the primary precursor for SO_4^{2-} production. Notably, WS also exerts a discernible positive contribution, suggesting a degree of regional transport influence during this episode, although its impact remains secondary to in situ chemical production. In contrast, RH exhibits no significant positive correlation with SO_4^{2-} and ranks relatively low in feature importance. Fe, a key catalyst for aqueous-phase SO_2 oxidation via Fenton-type chemistry (Ye et al., 2023b), likewise shows no clear positive association with SO_4^{2-}, with elevated ambient Fe concentrations not corresponding to enhanced sulfate formation. Taken together, these results indicate that aqueous-phase oxidation was not the dominant SO_4^{2-} formation pathway during the target episode. Meanwhile, O_3, VOCs, and alkene%, which serve as key proxies of gas-phase oxidant pathways, exhibit positive correlations with SO_4^{2-}, providing evidence that gas-phase oxidation constituted the primary sulfate formation pathway during this period. On this basis, ambient SO_4^{2-} concentrations can be regarded as a reliable observational proxy for the variability in total gas-phase H_2SO_4 production during the target episode.

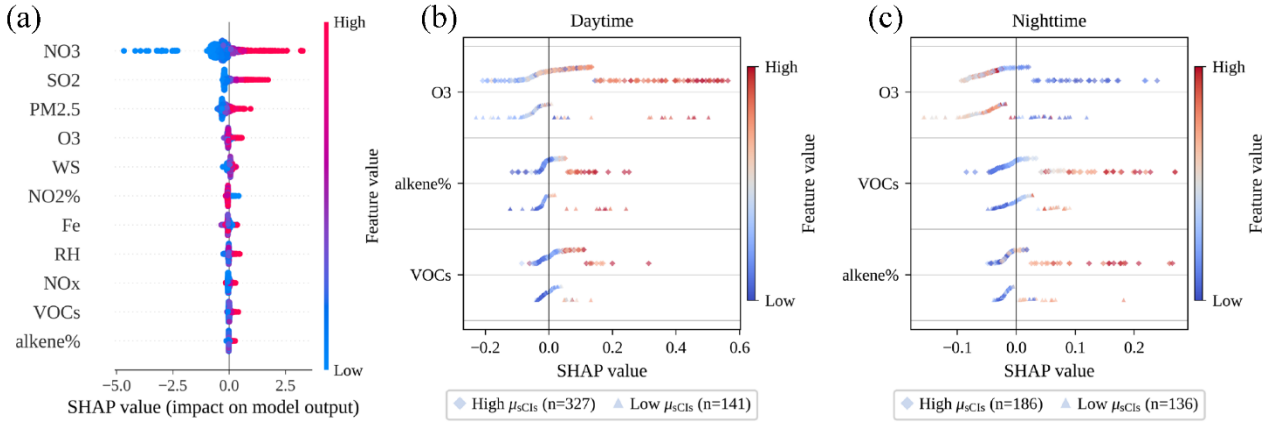

Figure 9. (a) SHAP beeswarm summary plot for the observation-based XGBoost model of ambient SO_4^{2-}. Each point represents one hourly observation, positioned according to the SHAP value of the corresponding predictor. Positive SHAP values indicate that the predictor increases the model-predicted SO_4^{2-} concentration, whereas negative values indicate a suppressing effect. Point colour denotes the predictor magnitude from low to high. Features are ordered by mean absolute SHAP value, so the plot summarizes both the relative importance and the directionality of the physically interpretable features. (b) Comparison of SHAP beeswarm plots for the observation-based XGBoost model under daytime low- and high-μ_{sCIs} regimes. Each point represents one hourly observation in the corresponding subset. The horizontal position gives the SHAP value, and the colour indicates the feature value. Differences between the two panels illustrate how the relative importance and directional effects of observed predictors on

ambient SO_4^{2-} vary between daytime chemical regimes with low and high inferred sCI contributions. (c) Comparison of SHAP beeswarm plots for the observation-based XGBoost model under nighttime low- and high-μ_{sCIs} regimes. Each point represents one hourly observation in the corresponding subset. The horizontal position gives the SHAP value, and the colour indicates the feature value. Differences between the two panels illustrate how the relative importance and directional effects of observed predictors on ambient SO_4^{2-} vary between nighttime chemical regimes with low and high inferred sCI contributions.

To further examine whether the sensitivity of SO_4^{2-} to key precursors is consistent with the regime-dependent behaviour of L_{SO2} identified in Sect. 3.2, the target episode was partitioned into high- and low-μ_{sCIs} subsets for daytime and nighttime periods separately, using the same classification thresholds applied in Section 3.2 (daytime: 1.1%; nighttime: 8.0%). SHAP values for O_3, VOCs, and alkene% were extracted for each subset and compared in Figures 9b and 9c. During daytime (Fig. 9b), the high-μ_{sCIs} subset exhibits systematically amplified SHAP responses relative to the low-μ_{sCIs} subset across all three precursors. O_3 shows the most pronounced regime contrast: in the high-μ_{sCIs} subset, high feature values (red) are associated with distinctly larger positive SHAP contributions and a considerably wider spread, whereas the corresponding responses in the low-μ_{sCIs} subset are substantially attenuated. VOCs and alkene% follow the same pattern, with high feature values driving larger positive SHAP contributions under high-μ_{sCIs} conditions. This daytime regime contrast is fully consistent with the finding in Sect. 3.2 that the sensitivity of SO_2 oxidation to O_3, VOCs, and alkene% is amplified under high-μ_{sCIs} conditions, and provides direct observational corroboration of that mechanistic result. At night (Fig. 9c), VOCs and alkene% exhibit stronger positive SHAP contributions to SO_4^{2-} in the high-μsCIs subset, consistent with their sustained roles as precursors to both sCIs and OH through nocturnal alkene ozonolysis. In contrast, O_3 exhibits negative SHAP contributions in both subsets, which can be attributed to the distinct behaviour of O_3 at night: nocturnal O_3 is primarily of advective origin rather than in situ photochemical production, and elevated O_3 concentrations are often associated with suppressed local NO levels due to rapid O_3-NO titration. Taken together, the regime-dependent SO_4^{2-} sensitivity patterns observed during the target episode (Figs. 9b, c) provide robust observational validation that the mechanistic findings derived from the process-model simulations in Sect. 3.2 are faithfully manifested in ambient atmospheric measurements. This cross-validation between model-diagnosed sensitivity and observation-based attribution reinforces the conclusion that under high-μsCIs regimes, alkene-targeted emission control strategies can effectively reduce sCIs and suppress the total SO_2 oxidation rate, and rarely cause rebound in OH-driven oxidation pathways.

4 Summary and conclusion

This study investigated the role of stabilised Criegee intermediates (sCIs) in gas-phase SO_2 oxidation by integrating updated chemical mechanism development, box-model simulations, interpretable machine learning, and ambient observations. The Master Chemical Mechanism (MCM v3.3.1) was revised to incorporate recent IUPAC kinetic recommendations for alkene ozonolysis and sCI chemistry, including unimolecular decomposition, stereoisomer-dependent reactivity, and competitive scavenging by H_2O and $(H_2O)_2$. The updated mechanism, MCM v3.3.1g, was implemented in the AtChem box model to generate simulation datasets under systematically perturbed chemical and meteorological conditions; these datasets were

subsequently used to train XGBoost surrogate models. XGBoost surrogate models were interpreted using SHAP attribution, Sobol sensitivity analysis, partial dependence plots, and and individual conditional expectation plots to quantify the controls on the absolute sCI-driven SO_2 oxidation rate, the fractional contribution of sCIs to total gas-phase SO_2 oxidation (μ_{sCIs}), and the sensitivity of total SO_2 oxidation under contrasting μsCIs regimes. The surrogate-derived sensitivity patterns were further evaluated using long-term hourly observations and a targeted summer episode in Wuhai.

The mechanism update substantially altered both the magnitude and attribution of sCI-mediated SO_2 oxidation. Relative to the original MCM v3.3.1, MCM v3.3.1g exhibited stronger sensitivity of the sCI-driven SO_2 oxidation rate to precursor and environmental perturbations, suggesting that the original mechanism underestimates the chemical responsiveness of the sCI pathway. More importantly, the update revised the inferred ranking of alkene precursors: isoprene emerged as the most influential species, followed by trans-2-butene, cis-2-butene, and 2-methylpropene, while ethene and propene/1-butene contributed only weakly across the investigated concentration ranges. This result demonstrates that alkene importance cannot be inferred from abundance, the ozonolysis rate constant, or bulk sCI yield alone, but is determined by the combined effects of ozonolysis kinetics, sCI yield, sCI speciation, the SO_2 reactivity of individual sCI species, and competitive removal by H_2O and $(H_2O)_2$. Relative humidity consistently suppressed the effective contribution of sCI to SO_2 oxidation, but the magnitude of this suppression depended strongly on the structure and fate of the sCIs produced.

The fractional contribution of sCIs to total gas-phase SO_2 oxidation was governed by the balance between sCI production and the competing OH-driven pathway. During the daytime, μ_{sCIs} was mainly enhanced by higher alkene ozonolysis reactivity (ARI), O_3, alkene fraction (alkene%), and total VOCs, whereas relative humidity suppressed μ_{sCIs} through enhanced $H_2O/(H_2O)_2$-driven sCI loss. NO_x and NO_2 fraction (NO_2%) had weaker independent effects, but their interaction effects were important because they regulate radical cycling, OH production, and termination. At night, the controlling factors shifted toward alkene reactivity, relative humidity, and NO_x, while the role of NO_2 fraction became negligible. This day–night contrast reflects the absence of photolysis at night, when alkene ozonolysis becomes an important source of both sCIs and primary OH. The μ_{sCIs} regime shaped the sensitivity of total gas-phase SO_2 oxidation (L_{SO2}) to precursor perturbations, with distinct daytime and nighttime behaviours. During the daytime, L_{SO2} responded positively on average to O_3, VOCs, and alkene% under both regimes, but the responses were stronger at high μ_{sCIs}. Negative responses occurred mainly under extremely low-NO_x level and were less frequent when μ_{sCIs} was high, because alkene ozonolysis provided concurrent sources of primary OH and sCIs that partly offset radical termination losses. At night, the regime dependence became more pronounced: O_3 and alkene% remained positively associated with L_{SO2} across most scenarios, whereas VOCs showed much stronger response heterogeneity under low-μ_{sCIs} regime, with the negative-slope fraction reaching 31% compared with 6% under high-μ_{sCIs} regime. This contrast reflects the dual role of nocturnal ozonolysis: when the ozonolysis pathway was weak, OH was sustained mainly by residual cycling within the non-alkene VOC pool, so a reduction in total VOCs lowered the OH sink, raised steady-state OH, and enhanced OH-driven SO_2 oxidation, producing negative L_{SO2}–VOCs slopes; when ozonolysis was strong, it simultaneously dominated sCI production and OH initiation, coupling the two oxidation channels such that precursor perturbations tend to drive L_{SO2} in the same direction, markedly reducing the

occurrence of negative responses. The lower frequency of negative responses for alkene fraction than for total VOCs across both regimes indicates that L_{SO2} is more robustly modulated by changes in the ozonolysis source.

The observation-based analysis provided support for the process-model results. During the selected Wuhai summer episode, SHAP analysis of the observation-based sulfate model showed that SO_2, O_3, VOCs, and alkene% were positively associated with particulate sulfate (SO_4^{2-}), whereas RH and Fe did not show evidence of dominant aqueous-phase sulfate production during the target period. This supports the use of ambient sulfate variability as an observational proxy for variability in total gas-phase H_2SO_4 production during this episode. Regime-separated SHAP analysis further showed that SO_4^{2-} responses to O_3, VOCs, and alkene% were amplified under high-μ_{sCIs} regime during the daytime, while nighttime SO_4^{2-} responses to VOCs and alkene% also strengthened when μ_{sCIs} was high. These observation-based patterns are broadly consistent with the regime-dependent sensitivities diagnosed from the AtChem surrogate models.

Overall, this work demonstrates that the atmospheric role of sCIs in SO_2 oxidation cannot be represented by a fixed contribution factor or by precursor abundance alone. Accurate assessment requires updated Criegee-intermediate kinetics, explicit consideration of alkene speciation, and a regime-aware treatment of the competition between sCI- and OH-driven oxidation. The results indicate that sCIs can substantially modulate the sensitivity of gas-phase sulfuric acid formation to O_3, VOCs, alkene composition, humidity, and NO_x, with distinct controlling structures during the day and at night. From an air-quality perspective, these findings suggest that alkene-targeted emission controls may be particularly effective under high-μ_{sCIs} regime, where reductions in reactive alkenes can simultaneously suppress sCI production and weaken total SO_2 oxidation, with a reduced likelihood of compensating OH-driven increases in SO_2 oxidation. The modelling and interpretation framework developed here can be extended to other atmospheric environments to evaluate the role of sCI chemistry in sulfate formation and new particle formation.

Data availability

The dataset used in this study is publicly available at: https://doi.org/10.5281/zenodo.17946348.

Supplement link

The link to the supplement will be included by Copernicus, if applicable.

Author contributions

YZ developed the methodology, performed data curation, visualization, formal analysis, and wrote the original draft. QC was responsible for conceptualization, formal analysis, funding acquisition, and reviewed and edited the manuscript. LH and WG participated in the revision of the manuscript. CS, DG, LJ and GY contributed to data curation.

Competing interests

The contact author has declared that none of the authors has any competing interests.

Disclaimer

Copernicus Publications remains neutral with regard to jurisdictional claims made in the text, published maps, institutional affiliations, or any other geographical representation in this paper. While Copernicus Publications makes every effort to include appropriate place names, the final responsibility lies with the authors. Views expressed in the text are those of the authors and do not necessarily reflect the views of the publisher.

Acknowledgements

This research was supported by the Lanzhou science and technology bureau, Project No. 2022-2-15, Research and Development of Key technologies for photocatalysis of low concentration organic waste Gas and the National Natural Science Foundation of China (grant no. 42305118). We thank the editors and anonymous reviewers for their valuable comments on the manuscript. During the preparation of this work, we used ChatGPT to proofread and refine the English expression of the manuscript. This included correcting grammatical errors, enhancing clarity, and improving the overall flow and coherence of the text. After using this tool, we reviewed and edited the content and take full responsibility for the content of the published article.

Financial support

The Lanzhou science and technology bureau, Project No. 2022-2-15, Research and Development of Key technologies for photocatalysis of low concentration organic waste Gas. The National Natural Science Foundation of China (grant no. 42305118).

References

Boy, M., Mogensen, D., Smolander, S., Zhou, L., Nieminen, T., Paasonen, P., Plass-Dülmer, C., Sipilä, M., Petäjä, T., Mauldin, L., Berresheim, H., and Kulmala, M.: Oxidation of SO2 by stabilized Criegee intermediate (sCI) radicals as a crucial source for atmospheric sulfuric acid concentrations, Atmos. Chem. Phys., 13, 3865–3879, https://doi.org/10.5194/acp-13-3865-2013, 2013.

Cao, J., Qiu, X., Gao, J., Wang, F., Wang, J., Wu, J., and Peng, L.: Significant decrease in SO2 emission and enhanced atmospheric oxidation trigger changes in sulfate formation pathways in China during 2008–2016, Journal of Cleaner Production, 326, 129396, https://doi.org/10.1016/j.jclepro.2021.129396, 2021.

Cao, J., Zheng, B., Chen, J., and Liu, Y.: Assessment of sulfate and nitrate variations in China during 1990 2020: Insights into source contributions and formation pathways, Journal of Hazardous Materials, 489, 137600, https://doi.org/10.1016/j.jhazmat.2025.137600, 2025.

Chen, T. and Guestrin, C.: XGBoost: A Scalable Tree Boosting System, in: Proceedings of the 22nd ACM SIGKDD International Conference on Knowledge Discovery and Data Mining, KDD '16: The 22nd ACM SIGKDD International Conference on Knowledge Discovery and Data Mining, San Francisco California USA, 785–794, https://doi.org/10.1145/2939672.2939785, 2016.

Cox, R. A. and Penkett, S. A.: Oxidation of Atmospheric SO2 by Products of the Ozone–Olefin Reaction, Nature, 230, 321–322, https://doi.org/10.1038/230321a0, 1971.

Cox, R. A., Ammann, M., Crowley, J. N., Herrmann, H., Jenkin, M. E., McNeill, V. F., Mellouki, A., Troe, J., and Wallington, T. J.: Evaluated kinetic and photochemical data for atmospheric chemistry: Volume VII – Criegee intermediates, Atmos. Chem. Phys., 20, 13497–13519, https://doi.org/10.5194/acp-20-13497-2020, 2020.

Dada, L., Ylivinkka, I., Baalbaki, R., Li, C., Guo, Y., Yan, C., Yao, L., Sarnela, N., Jokinen, T., Daellenbach, K. R., Yin, R., Deng, C., Chu, B., Nieminen, T., Wang, Y., Lin, Z., Thakur, R. C., Kontkanen, J., Stolzenburg, D., Sipilä, M., Hussein, T., Paasonen, P., Bianchi, F., Salma, I., Weidinger, T., Pikridas, M., Sciare, J., Jiang, J., Liu, Y., Petäjä, T., Kerminen, V.-M., and Kulmala, M.: Sources and sinks driving sulfuric acid concentrations in contrasting environments: implications on proxy calculations, Atmos. Chem. Phys., 20, 11747–11766, https://doi.org/10.5194/acp-20-11747-2020, 2020.

Dai, Q., Bi, X., Song, W., Li, T., Liu, B., Ding, J., Xu, J., Song, C., Yang, N., Schulze, B. C., Zhang, Y., Feng, Y., and Hopke, P. K.: Residential coal combustion as a source of primary sulfate in Xi'an, China, Atmospheric Environment, 196, 66–76, https://doi.org/10.1016/j.atmosenv.2018.10.002, 2019.

Gao, J., Li, Y., Li, J., Shi, G., Liu, Z., Han, B., Tian, X., Wang, Y., Feng, Y., and Russell, A. G.: Impact of Formation Pathways on Secondary Inorganic Aerosol During Haze Pollution in Beijing: Quantitative Evidence From High-Resolution Observation and Modeling, Geophysical Research Letters, 48, e2021GL095623, https://doi.org/10.1029/2021GL095623, 2021.

Geng, G., Zheng, Y., Zhang, Q., Xue, T., Zhao, H., Tong, D., Zheng, B., Li, M., Liu, F., Hong, C., He, K., and Davis, S. J.: Drivers of PM2.5 air pollution deaths in China 2002–2017, Nat. Geosci., 14, 645–650, https://doi.org/10.1038/s41561-021-00792-3, 2021.

Goldstein, A., Kapelner, A., Bleich, J., and Pitkin, E.: Peeking Inside the Black Box: Visualizing Statistical Learning With Plots of Individual Conditional Expectation, Journal of Computational and Graphical Statistics, 24, 44–65, https://doi.org/10.1080/10618600.2014.907095, 2015.

Gunthe, S. S., Rose, D., Su, H., Garland, R. M., Achtert, P., Nowak, A., Wiedensohler, A., Kuwata, M., Takegawa, N., Kondo, Y., Hu, M., Shao, M., Zhu, T., Andreae, M. O., and Pöschl, U.: Cloud condensation nuclei (CCN) from fresh and aged air pollution in the megacity region of Beijing, Atmos. Chem. Phys., 11, 11023–11039, https://doi.org/10.5194/acp-11-11023-2011, 2011.

Guo, Y., Yan, C., Li, C., Ma, W., Feng, Z., Zhou, Y., Lin, Z., Dada, L., Stolzenburg, D., Yin, R., Kontkanen, J., Daellenbach, K. R., Kangasluoma, J., Yao, L., Chu, B., Wang, Y., Cai, R., Bianchi, F., Liu, Y., and Kulmala, M.: Formation of nighttime sulfuric acid from the ozonolysis of alkenes in Beijing, Atmos. Chem. Phys., 21, 5499–5511, https://doi.org/10.5194/acp-21-5499-2021, 2021.

H. Khan, M. A., Morris, W. C., Galloway, M., A. Shallcross, B. M., Percival, C. J., and Shallcross, D. E.: An Estimation of the Levels of Stabilized Criegee Intermediates in the UK Urban and Rural Atmosphere Using the Steady-State Approximation and the Potential Effects of These Intermediates on Tropospheric Oxidation Cycles: AN ESTIMATION OF THE LEVELS OF STABILIZED CRIEGEE INTERMEDIATES IN THE UK, Int. J. Chem. Kinet., 49, 611–621, https://doi.org/10.1002/kin.21101, 2017.

Hata, H., Hoshino, S., Fujita, M., and Tonokura, K.: Atmospheric impact of isoprene-derived Criegee intermediates and isoprene hydroxy hydroperoxide on sulfate aerosol formation in the Asian region, Atmospheric Environment: X, 20, 100226, https://doi.org/10.1016/j.aeaoa.2023.100226, 2023.

Herman, J. and Usher, W.: SALib: An open-source Python library for Sensitivity Analysis, JOSS, 2, 97, https://doi.org/10.21105/joss.00097, 2017.

Jenkin, M. E., Saunders, S. M., and Pilling, M. J.: The tropospheric degradation of volatile organic compounds: a protocol for mechanism development, Atmospheric Environment, 31, 81–104, https://doi.org/10.1016/S1352-2310(96)00105-7, 1997.

Jenkin, M. E., Young, J. C., and Rickard, A. R.: The MCM v3.3.1 degradation scheme for isoprene, Atmos. Chem. Phys., 15, 11433–11459, https://doi.org/10.5194/acp-15-11433-2015, 2015.

Khan, M. A. H., Percival, C. J., Caravan, R. L., Taatjes, C. A., and Shallcross, D. E.: Criegee intermediates and their impacts on the troposphere, Environ. Sci.: Processes Impacts, 20, 437–453, https://doi.org/10.1039/C7EM00585G, 2018.

Kim, S., Guenther, A., Lefer, B., Flynn, J., Griffin, R., Rutter, A. P., Gong, L., and Cevik, B. K.: Potential Role of Stabilized Criegee Radicals in Sulfuric Acid Production in a High Biogenic VOC Environment, Environ. Sci. Technol., 49, 3383–3391, https://doi.org/10.1021/es505793t, 2015.

Kukui, A., Chartier, M., Wang, J., Chen, H., Dusanter, S., Sauvage, S., Michoud, V., Locoge, N., Gros, V., Bourrianne, T., Sellegri, K., and Pichon, J.-M.: Role of Criegee intermediates in the formation of sulfuric acid at a Mediterranean (Cape Corsica) site under influence of biogenic emissions, Atmos. Chem. Phys., 21, 13333–13351, https://doi.org/10.5194/acp-21-13333-2021, 2021a.

Kukui, A., Chartier, M., Wang, J., Chen, H., Dusanter, S., Sauvage, S., Michoud, V., Locoge, N., Gros, V., Bourrianne, T., Sellegri, K., and Pichon, J.-M.: Role of Criegee intermediates in the formation of sulfuric acid at a Mediterranean (Cape Corsica) site under influence of biogenic emissions, Atmos. Chem. Phys., 21, 13333–13351, https://doi.org/10.5194/acp-21-13333-2021, 2021b.

Lade, R. E., Blitz, M. A., Rowlinson, M., Evans, M. J., Seakins, P. W., and Stone, D.: Kinetics of the reactions of the Criegee intermediate CH_2 OO with water vapour: experimental measurements as a function of temperature and global atmospheric modelling, Environ. Sci.: Atmos., 4, 1294–1308, https://doi.org/10.1039/D4EA00097H, 2024.

Li, J., Ying, Q., Yi, B., and Yang, P.: Role of stabilized Criegee Intermediates in the formation of atmospheric sulfate in eastern United States, Atmospheric Environment, 79, 442–447, https://doi.org/10.1016/j.atmosenv.2013.06.048, 2013.

Lundberg, S. M. and Lee, S.-I.: A Unified Approach to Interpreting Model Predictions, 2017.

Lundberg, S. M., Nair, B., Vavilala, M. S., Horibe, M., Eisses, M. J., Adams, T., Liston, D. E., Low, D. K.-W., Newman, S.-F., Kim, J., and Lee, S.-I.: Explainable machine-learning predictions for the prevention of hypoxaemia during surgery, Nat Biomed Eng, 2, 749–760, https://doi.org/10.1038/s41551-018-0304-0, 2018.

Lundberg, S. M., Erion, G., Chen, H., DeGrave, A., Prutkin, J. M., Nair, B., Katz, R., Himmelfarb, J., Bansal, N., and Lee, S.-I.: From local explanations to global understanding with explainable AI for trees, Nat Mach Intell, 2, 56–67, https://doi.org/10.1038/s42256-019-0138-9, 2020.

Mauldin, R. L., Berndt, T., Sipilä, M., Paasonen, P., Petäjä, T., Kim, S., Kurtén, T., Stratmann, F., Kerminen, V.-M., and Kulmala, M.: A new atmospherically relevant oxidant of sulphur dioxide, Nature, 488, 193–196, https://doi.org/10.1038/nature11278, 2012.

Meidan, D., Holloway, J. S., Edwards, P. M., Dubé, W. P., Middlebrook, A. M., Liao, J., Welti, A., Graus, M., Warneke, C., Ryerson, T. B., Pollack, I. B., Brown, S. S., and Rudich, Y.: Role of Criegee Intermediates in Secondary Sulfate Aerosol Formation in Nocturnal Power Plant Plumes in the Southeast US, ACS Earth and Space Chemistry, 2019.

Newland, M. J., Rickard, A. R., Alam, M. S., Vereecken, L., Muñoz, A., Ródenas, M., and Bloss, W. J.: Kinetics of stabilised Criegee intermediates derived from alkene ozonolysis: reactions with SO_2 , H_2 O and decomposition under boundary layer conditions, Phys. Chem. Chem. Phys., 17, 4076–4088, https://doi.org/10.1039/C4CP04186K, 2015.

Quaas, J., Jia, H., Smith, C., Albright, A. L., Aas, W., Bellouin, N., Boucher, O., Doutriaux-Boucher, M., Forster, P. M., Grosvenor, D., Jenkins, S., Klimont, Z., Loeb, N. G., Ma, X., Naik, V., Paulot, F., Stier, P., Wild, M., Myhre, G., and Schulz, M.: Robust evidence for reversal of the trend in aerosol effective climate forcing, Atmos. Chem. Phys., 22, 12221–12239, https://doi.org/10.5194/acp-22-12221-2022, 2022.

Ruscic, B.: Active Thermochemical Tables: Water and Water Dimer, J. Phys. Chem. A, 117, 11940–11953, https://doi.org/10.1021/jp403197t, 2013.

Saltelli, A.: Making best use of model evaluations to compute sensitivity indices, Computer Physics Communications, 145, 280–297, https://doi.org/10.1016/S0010-4655(02)00280-1, 2002.

Saltelli, A., Annoni, P., Azzini, I., Campolongo, F., Ratto, M., and Tarantola, S.: Variance based sensitivity analysis of model output. Design and estimator for the total sensitivity index, Computer Physics Communications, 181, 259–270, https://doi.org/10.1016/j.cpc.2009.09.018, 2010.

Sarwar, G., Simon, H., Fahey, K., Mathur, R., Goliff, W. S., and Stockwell, W. R.: Impact of sulfur dioxide oxidation by Stabilized Criegee Intermediate on sulfate, Atmospheric Environment, 85, 204–214, https://doi.org/10.1016/j.atmosenv.2013.12.013, 2014.

Saunders, S. M., Jenkin, M. E., Derwent, R. G., and Pilling, M. J.: Protocol for the development of the Master Chemical Mechanism, MCM v3 (Part A): tropospheric degradation of non-aromatic volatile organic compounds, Atmos. Chem. Phys., 3, 161–180, https://doi.org/10.5194/acp-3-161-2003, 2003.

Scribano, Y., Goldman, N., Saykally, R. J., and Leforestier, C.: Water Dimers in the Atmosphere III: Equilibrium Constant from a Flexible Potential, J. Phys. Chem. A, 110, 5411–5419, https://doi.org/10.1021/jp056759k, 2006.

Sheehy, P. M., Volkamer, R., Molina, L. T., and Molina, M. J.: Oxidative capacity of the Mexico City atmosphere – Part 2: A RO_x radical cycling perspective, Atmos. Chem. Phys., 10, 6993–7008, https://doi.org/10.5194/acp-10-6993-2010, 2010.

Sobol, I. M.: Global sensitivity indices for nonlinear mathematical models and their Monte Carlo estimates, Mathematics and Computers in Simulation, 55, 271–280, https://doi.org/10.1016/S0378-4754(00)00270-6, 2001.

Sommariva, R., Cox, S., Martin, C., Borońska, K., Young, J., Jimack, P. K., Pilling, M. J., Matthaios, V. N., Nelson, B. S., Newland, M. J., Panagi, M., Bloss, W. J., Monks, P. S., and Rickard, A. R.: AtChem (version 1), an open-source box model for the Master Chemical Mechanism, Geosci. Model Dev., 13, 169–183, https://doi.org/10.5194/gmd-13-169-2020, 2020.

Song, X., Yi, J., Chen, Y., Su, Y., Wang, H., Liu, A., Wu, D., and Li, Q.: Condensable particulate matter emissions regulated by flue gas desulfurization technologies in typical industrial plants, Journal of Hazardous Materials, 489, 137527, https://doi.org/10.1016/j.jhazmat.2025.137527, 2025.

Taatjes, C. A., Welz, O., Eskola, A. J., Savee, J. D., Scheer, A. M., Shallcross, D. E., Rotavera, B., Lee, E. P. F., Dyke, J. M., Mok, D. K. W., Osborn, D. L., and Percival, C. J.: Direct Measurements of Conformer-Dependent Reactivity of the Criegee Intermediate CH_3 CHOO, Science, 340, 177–180, https://doi.org/10.1126/science.1234689, 2013.

Vereecken, L., Harder, H., and Novelli, A.: The reaction of Criegee intermediates with NO, RO2, and SO2, and their fate in the atmosphere, Phys. Chem. Chem. Phys., 14, 14682, https://doi.org/10.1039/c2cp42300f, 2012.

Vereecken, L., Novelli, A., and Taraborrelli, D.: Unimolecular decay strongly limits the atmospheric impact of Criegee intermediates, Phys. Chem. Chem. Phys., 19, 31599–31612, https://doi.org/10.1039/C7CP05541B, 2017.

Wang, Z., Nie, W., Liu, Y., Yang, L., Liu, C., Zhang, Y., Yan, C., Zha, Q., Ge, D., Qi, X., Zhou, C., Chen, L., Zhou, X., Wang, L., Huang, D. D., Chi, X., and Ding, A.: Gaseous Sulfuric Acid Contributions to Sulfate Formation in Urban Atmosphere, Environ. Sci. Technol. Lett., 12, 189–195, https://doi.org/10.1021/acs.estlett.4c01028, 2025.

WHO: WHO Global Air Quality Guidelines: Particulate Matter (PM2. 5 and PM10), Ozone, Nitrogen Dioxide, Sulfur Dioxide and Carbon Monoxide, 1st ed., World Health Organization, Geneva, 1 pp., 2021.

Yao, L., Garmash, O., Bianchi, F., Zheng, J., Yan, C., Kontkanen, J., Junninen, H., Mazon, S. B., Ehn, M., Paasonen, P., Sipilä, M., Wang, M., Wang, X., Xiao, S., Chen, H., Lu, Y., Zhang, B., Wang, D., Fu, Q., Geng, F., Li, L., Wang, H., Qiao, L., Yang, X., Chen, J., Kerminen, V.-M., Petäjä, T., Worsnop, D. R., Kulmala, M., and Wang, L.: Atmospheric new particle formation from sulfuric acid and amines in a Chinese megacity, Science, 361, 278–281, https://doi.org/10.1126/science.aao4839, 2018.

Ye, C., Lu, K., Song, H., Mu, Y., Chen, J., and Zhang, Y.: A critical review of sulfate aerosol formation mechanisms during winter polluted periods, Journal of Environmental Sciences, 123, 387–399, https://doi.org/10.1016/j.jes.2022.07.011, 2023a.

Ye, C., Lu, K., Song, H., Mu, Y., Chen, J., and Zhang, Y.: A critical review of sulfate aerosol formation mechanisms during winter polluted periods, Journal of Environmental Sciences, 123, 387–399, https://doi.org/10.1016/j.jes.2022.07.011, 2023b.

Zhu, T., Tang, M., Gao, M., Bi, X., Cao, J., Che, H., Chen, J., Ding, A., Fu, P., Gao, J., Gao, Y., Ge, M., Ge, X., Han, Z., He, H., Huang, R.-J., Huang, X., Liao, H., Liu, C., Liu, H., Liu, J., Liu, S. C., Lu, K., Ma, Q., Nie, W., Shao, M., Song, Y., Sun, Y., Tang, X., Wang, T., Wang, T., Wang, W., Wang, X., Wang, Z., Yin, Y., Zhang, Q., Zhang, W., Zhang, Y., Zhang, Y., Zhao, Y., Zheng, M., Zhu, B., and Zhu, J.: Recent Progress in Atmospheric Chemistry Research in China: Establishing a Theoretical Framework for the “Air Pollution Complex,” Adv. Atmos. Sci., 40, 1339–1361, https://doi.org/10.1007/s00376-023-2379-0, 2023.